FY22 Laboratory Basic Science Program

M. S. Wei

Laboratory for Laser Energetics, University of Rochester

The Laboratory Basic Science (LBS) Program awarded 21 projects with a total allocation of 22 shot days for a full-year schedule at the Omega Laser Facility in FY22 including six carryover FY21 LBS projects with shots in Q1FY22. A total of 224 target shots were conducted for the LBS Program in FY22. These experiments were led by scientists from Lawrence Livermore National Laboratory (LLNL), SLAC, Princeton Plasma Physics Laboratory (PPPL), and LLE (see Table I). The LBS experiments conducted in FY22 are summarized in this section.

During FY22, LLE issued a solicitation for LBS proposals for beam time in FY23. A total of 20 proposals were submitted, requesting a total of 30 Omega shot days, which was about 150% of the notional allocation for the LBS Program. The reduced number of proposals compared to prior years was attributed to several factors including an early deadline (by a month due to the change of the annual Omega Scheduling meeting from June 2022 to May 2022) and many overlapping activities such as proposals to the High-Energy-Density (HED) Council for shots at the National Ignition Facility and white papers for the Laboratory Directed Research and Development (LDRD) Program at LLNL, among others. An independent LBS Proposal Review Panel (PRP) consisting of eight subject-matter experts from universities, national laboratories, and industry reviewed and ranked the proposals. Based on the LBS PRP's recommendation, 19 proposals were selected and allocated a total of 21.5 shot days for experiments at the Omega Laser Facility in FY23, as shown in Table II.

Table I: LBS Projets with experiments conducted at the Omega Laser Facility in FY22, including six carryovers from the FY21 LBS Program (gray shaded cells).

Principal Investigator	Lead Institution	Title
H. Chen/M. R. Edwards	LLNL/Stanford Univeristy	Developing a Magnetic Mirror Trap for Laser-Produced Relativistic Electron–Positron Pairs/Exploring Electron and Electron–Positron Plasma Dynamics
H. Chen/G. Gregori	LLNL/University of Oxford	Measuring Particle Transport in Turbulent Plasmas/Laboratory Model of Particle Acceleration in Supernova Shocks
F. Coppari/Y. Kim	LLNL	Measurements of Shock Equation of State and Melting Temperature of H:N:O and H:C:N:O Mixtures
L. Gao	PPPL	Particle Acceleration from Magnetically Driven Collisionless Reconnection Using Short-Pulse, Laser-Powered Capacitor Coils
H. G. Rinderknecht	LLE	Initial Relativistically Transparent Microchannel Experiments on OMEGA EP
A. Zylstra/J. Jeet	LLNL	Inertial Confinement Fusion Plasma-Based Measurements of the T + ^{4}He Cross Section
F. Albert	LLNL	High-Precision X-Ray Radiography Driven by Laser Wakefield Acceleration/X-Ray Sources from Laser Wakefield Acceleration on OMEGA EP

Table I: LBS Projets with experiments conducted at the Omega Laser Facility in FY22, including six carryovers from the FY21 LBS Program (gray shaded cells) (continued).

Principal Investigator	Lead Institution	Title
G. Bruhaug	LLE	Relativistic THz-Matter Interactions/Extreme THz Generation and Detection
G. W. Collins/ A. Schwemmlein	LLE	Quantum States of Hydrogen: Toward a Superconducting Superfluid
A. Gleason	SLAC	Viscosity Measurements Using Tracer Particles
I. V. Igumenshchev/ V. N. Goncharov	LLE	Formation of Dynamic Shells Using Foam Ball Targets
J. Jeet	LLNL	Cross-Calibration of the D–T γ-to-Neutron and D–^{3}He γ-to-Protron Branching Ratios Against the ^{12}C(n,n$'$)γ Reaction/Inertial Confinement Fusion Plasma-Based Measurements of the D–T γ-to-Neutron and D–^{3}He γ-to-Protron Branching Ratios
S. Malko	PPPL	Detailed Benchmarking of the Nernst Effect in a Magnetized High-Energy-Density Plasma
J. L. Peebles	LLE	Probing In-Flight Vacuum Magnetic-Field Compression on OMEGA
M. J. Rosenberg	LLE	Electron Energization in Colliding and Reconnecting Magnetized Plasmas
M. Schneider	LLNL	Using Isoelectronic Line Ratios to Measure Density in Nonlocal Thermodynamic Equilibrium Plasmas/Measuring Electron Densities in Nonlocal Thermodynamic Equilibrium Plasmas Using Isoelectronic Line Ratios
S. Singh/S. Clarke	LLNL	The Effect of Ni Concentration on Phase Transformation Dynamics in the Fe-Ni Binary System/Probing the Fe–Ni Phase Space Using Powder X-Ray Diffraction Image Plates
R. F. Smith	LLNL	Measuring the Viscosity of MgO at Lower-Mantle Conditions
C. Stoeckl/A. Schwemmlein	LLE	Development of a New Experimental Platform LIANS on OMEGA EP for Deuteron and Triton-Induced Nuclear Reactions—Studying the T–T Reaction at Energies Exceeding 2 MeV on OMEGA
G. Swadling	LLNL	Angular Momentum Transport in Disk-Jet Transitions

Table II: Nineteen projects from the FY23 LBS Program approved for target shots at the Omega Laser Facility in FY23.

Principal Investigator	Lead Institution	Title
F. Albert	LLNL	X-Ray Radiography of Laser-Driven Shocks Using Laser Wakefield Acceleration
L. Ceurvorst	LLE	Amplification of Laser Imprint with Strong Magnetic Fields
K. Churnetski	LLE	Evaluating Shock-Augmented Ignition and Late-Time Laser–Capsule Coupling in Laser Inertial Fusion
G. W. Collins	LLE	Quantum States of Hydrogen: Toward a Superconducing Superfluid
J. R. Davies	LLE	Measurement of a Self-Generated Magnetic Field in Laser–Foil Interactions with Oblique Proton Probing
C. J. Forrest	LLE	Multiple Reactant Implosions to Improve Cross-Section Measurements of Reactions Relevant to Nuclear Astrophysics
L. Gao	PPPL	Multi-Scale Reconnection and Particle Acceleration in Long Current Sheets During Magnetically Driven Collisionless Reconnection at Low Plasma β

Table II: Nineteen projects from the FY23 LBS Program approved for target shots at the Omega Laser Facility in FY23 (continued).

Principal Investigator	Institution	Title
F. García-Rubio	LLE	Driving Magnetized Collisionless Shocks with Solid Pistons on OMEGA EP
A. Gleason	SLAC	Particle Tracking in High-Energy-Density Flows
D. Haberberger	LLE	Raman Pump Propagation
P. V. Heuer	LLE	Benchmarking Nernst Advection in Local and Nonlocal Regimes
M. Holec	LLNL	Nonlocal Electron Transport in Collisional Magnetized Plasma Jets
Y. Kim	LANL	Development of an Ion Stopping-Power Platform at Low Projectile-to-Thermal Velocity Ratio
S. Malko	PPPL	Proton Radiography of a Bounded, Magnetized Plasma Relevant to MagLIF
J. L. Peebles	LLE	Measurement and Application of Short-Pulse Compressed Magnetic Field
M. Sherlock	LLNL	Study of Magnetization Effects in Cylindrically Imploded Hot Dense Plasmas Using Dopant Spectroscopy Techniques
R. Smith	LLNL	Novel Experiments to Measure Viscosity of Minerals at the Conditions of Planetary Interiors
C. Stoeckl	LLE	Investigating the Dynamics and Stability of Astrophysical-Relevant Plasma Jets
G. Swadling	LLNL	Effects of Collisionality in Angular Momentum Transport in Disk-Jet Transitions

Exploring Electron and Electron–Positron Plasma Dynamics

M. R. Edwards,[1*] S. You,[2] J. von der Linden,[3] J. L. Peebles,[4] L. Willingale,[5] G. Fiksel,[5] and H. Chen[2*]
[1]Stanford University
[2]Lawrence Livermore National Laboratory
[3]Max Planck Institute for Plasma Physics
[4]Laboratory for Laser Energetics, University of Rochester
[5]University of Michigan
[*]Principal Investigators

To explore instabilities of relativistic electron and electron–positron beams, this experiment aimed to collide a relativistic electron–positron jet with a low-density hydrocarbon plasma and examine the interaction region for the development of magnetic-field filaments. This work aims both to understand the fundamental properties of electron and electron–positron plasmas and to explore possible scaled experiments with astrophysical relevance.

In the experiment, electron–positron jets were produced by focusing the backlighter beam on specially designed large-diameter gold-copper targets that controlled the positron acceleration. A background plasma was generated using Beam 3 on a hydrocarbon disk target. The interaction zone was imaged with sidelighter-driven proton radiography and the properties of the jet were characterized with an electron–proton–positron spectrometer (EPPS). We used the magneto-inertial fusion electrical discharge system (MIFEDS) to control the focusing of low-energy electrons and positrons into the interaction zone.

Particle spectrometer measurements confirmed control over positron energy using large-diameter targets and control over low-energy electron and positron focusing using MIFEDS. We observed the development of large-scale instabilities (Fig. 1), suggesting the presence of an electron-driven instability. These results suggest progress toward a platform for studying relativistic electron jet instabilities using kilojoule-class lasers.

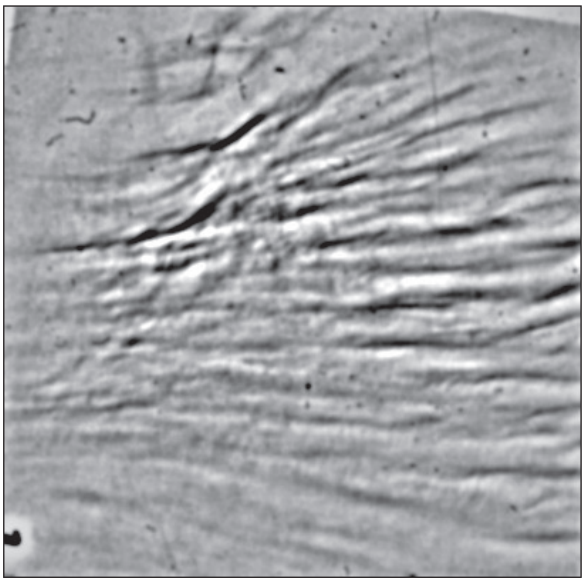

U2900JR

Figure 1
Filtered proton radiography image-plate data showing evidence of instability development in an electron beam crossing a background plasma.

Laboratory Model of Particle Acceleration in Supernova Shocks

H. Chen,[1*] C. A. J. Palmer,[2] H. Poole,[3] A. R. Bell,[3] A. Bott,[4] G. Gregori,[3*] O. Karnbach,[3] J. Matthews,[3] D. Lamb,[5] R. D. Petrasso,[6] P. Tzeferacos,[7] A. Birkel,[6] C. K. Li,[6] and H.-S. Park[1]
[1]Lawrence Livermore National Laboratory
[2]Queen's University, Belfast, UK
[3]University of Oxford, UK
[4]Princeton University
[5]University of Chicago
[6]Massachusetts Institute of Technology
[7]Laboratory for Laser Energetics, University of Rochester
[*]Principal Investigator

Magneto-collisional instabilities (MCI's) have been proposed as an explanation for the observation of acceleration of cosmic rays (CR's) to energies higher than those predicted by simple models in the turbulent magnetized plasmas surrounding supernova remnants. The instabilities, driven by high-intensity currents of CR's, can lead to amplification of the plasma magnetic fields, which results in prolonged trapping of the energetic CR in the turbulent plasma and, consequently, higher maximum energies. This is particularly true for a subset of these instabilities, the "nonresonant hybrid instability," which drives the growth of fields at the scale of the Larmor radius of the CR current. Due to the nature of this instability, covering a high dynamic range of spatial and temporal scales and requiring the inclusion of kinetic processes, computational simulations struggle to accurately model the process.

A joint shot day at LLE in 2019 aimed to explore this field amplification in the laboratory using the well-established turbulent dynamo target platform (TDYNO) to create a turbulent plasma embedded with stochastic magnetic fields, and a high-energy (2-kJ), short-pulse (100-ps) OMEGA EP laser beam to produce a high-intensity proton current that would drive the instability (Fig. 2). The results of this shot day indicated the generation of a >1-kA proton beam with a cutoff energy of approximately 3 MeV, which was only detected when the turbulent plasma was not present.

This may indicate MCI's inhibition of the proton propagation or disruption to the proton-generation mechanism due to the close proximity of the proton source to the turbulent plasmas. Follow-up experiments in 2021 aimed to directly compare the density and magnetic-field structure of the plasma turbulence with and without a high-current drive beam, as well as test for confirmation signatures of proton production using a modified target design. As in 2019, the main diagnostics included an x-ray framing camera to measure self-emission from the turbulent plasma, proton radiography using a D^3He capsule irradiated with 17 OMEGA beams

(450 J/beam, 1 ns) to probe the magnetic-field structure of the plasma, the EPPS to measure the energy spectrum of the target normal sheath acceleration (TNSA) proton beam, and the Zinc von Hamos spectrometer to measure protons induced x-ray emission from a tracer foil on the proton-generation target.

Data were obtained for a direct comparison on the proton radiography and x-ray self-emission with and without the high-current instability drive beam. This confirmed that a change in structure of the x-ray self-emission from the standard TDYNO plasma, observed in 2019, was not due to the presence of the proton beam, but likely due to a small change in ordering and therefore orientation of the TDYNO drive beam (Fig. 3). This is being investigated further using the radiation hydrocode *FLASH*.

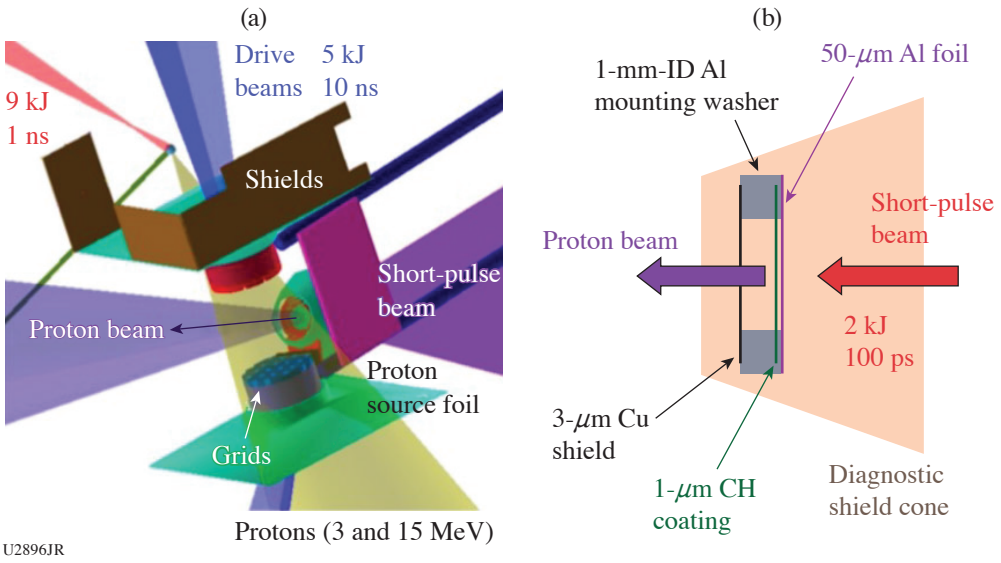

Figure 2
(a) Experimental configuration and (b) a TNSA target. The EPPS diagnostic sits along the axis of the marked proton beam.

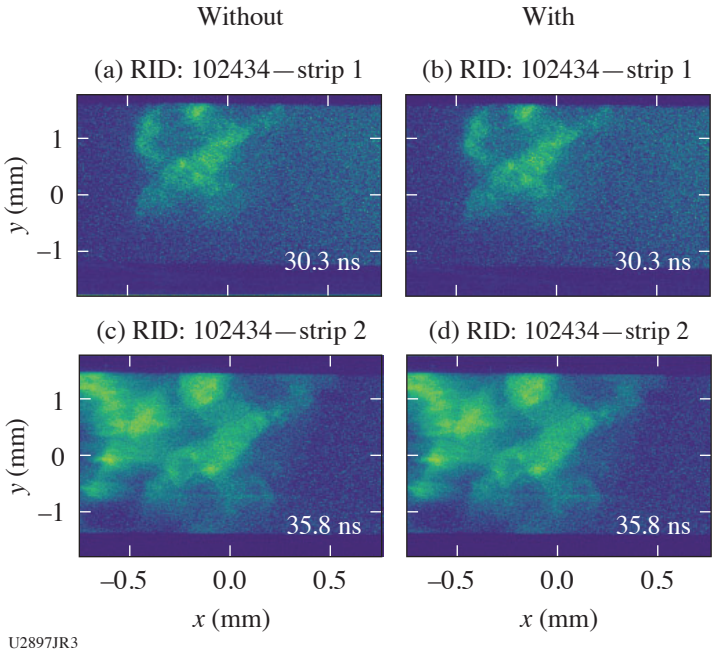

Figure 3
Comparison of the evolution of the plasma density structure via the x-ray self-emission measured at two times, 30.3 ns and 35.8 ns, respectively, for shots [(a) and (c)] without or [(b) and (d)] with the high-energy OMEGA EP interaction. While the structure is qualitatively different from typical TDYNO data, with a central hole, the two shots here do not indicate that structural changes are due to the propagation of a high-current proton beam.

The zinc von Hamos spectrometer suffered from strong continuum background due to the capsule drive, but the spectra indicated the presence of several lines consistent with copper emission, which is most clearly visible on shots without the D^3He backlighter capsule or turbulent plasma (Fig. 4). Analysis is ongoing to determine whether this diagnostic can confirm that proton-beam acceleration is not prevented by the presence of the turbulent plasma.

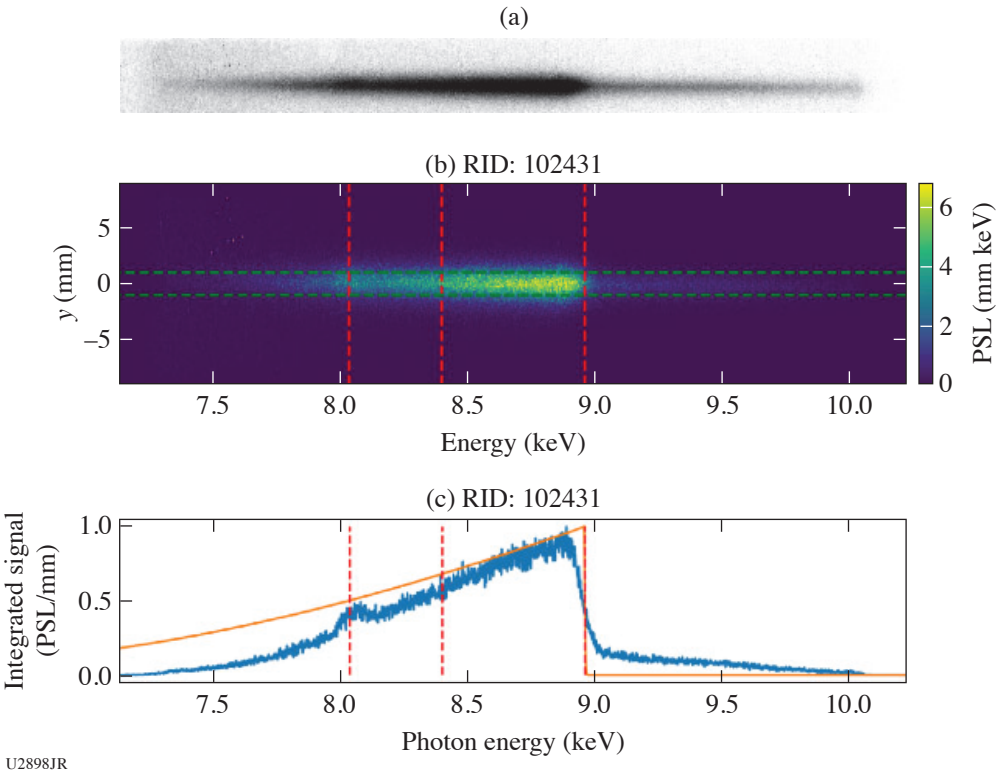

Figure 4
Zinc von Hamos spectra from an OMEGA EP shot showing (a) the raw data, (b) processed image, and (c) an integrated signal lineout, which indicates excess emission consistent with copper K_α emission with only the copper in the target included in the tracer layer of the OMEGA EP target.

Measurements of Shock Equation of State and Melting Temperature of H:N:O and H:C:N:O Mixtures

Y.-J. Kim,[1] M. Bethkenhagen,[2] S. Hamel,[1] M. Wadas,[3] S. Stanley,[4] M. Millot,[1] and F. Coppari[1*]
[1]Lawrence Livermore National Laboratory
[2]Rostock University, Germany
[3]University of Michigan
[4]Johns Hopkins University
[*]Principal Investigator

This ExtChmDAC-21 campaign under the support of the LBS Program aims at investigating the optical and thermodynamic properties of ammonia-rich H:N:O and synthetic Uranus (SU) H:C:N:O mixtures at the extreme pressure–temperature conditions that we expect in the deep interior of icy giant planets such as Uranus and Neptune. This work expands on our recent discovery of superionic water ice (or ice XVIII)[1–3] to reveal the possible existence of the superionic phase in the icy planet constituents as well as its melting temperature.

We prepared ammonia monohydrate (AMH, $NH_3{\cdot}H_2O$), ammonia hemihydrate (AHH, $2NH_3{\cdot}H_2O$), and SU mixtures, and documented their optical properties at the ambient condition.[4] These liquid mixtures were precompressed to 1 to 2 GPa in diamond anvil cells (DAC's) to increase their initial density at room temperature, achieve lower temperatures but higher compression under dynamic loading, and finally reach planetary interior conditions. With excellent laser performance and support, we collected 14 system shots in the one-day allocation. Doppler velocimetry (VISAR) and streaked optical pyrometry (SOP) were used to track the shock-wave propagation through the precompressed sample and to document the pressure–density–temperature shock equation of state as well as the evolution of the optical properties (reflectivity, absorption coefficient) along the shock Hugoniot curves using a quartz reference (see Fig. 5) (Refs. 5,6). The ongoing data analysis will be used to improve our understanding of chemical bonding changes in this regime and benchmark future improved equation-of-state and planetary models.

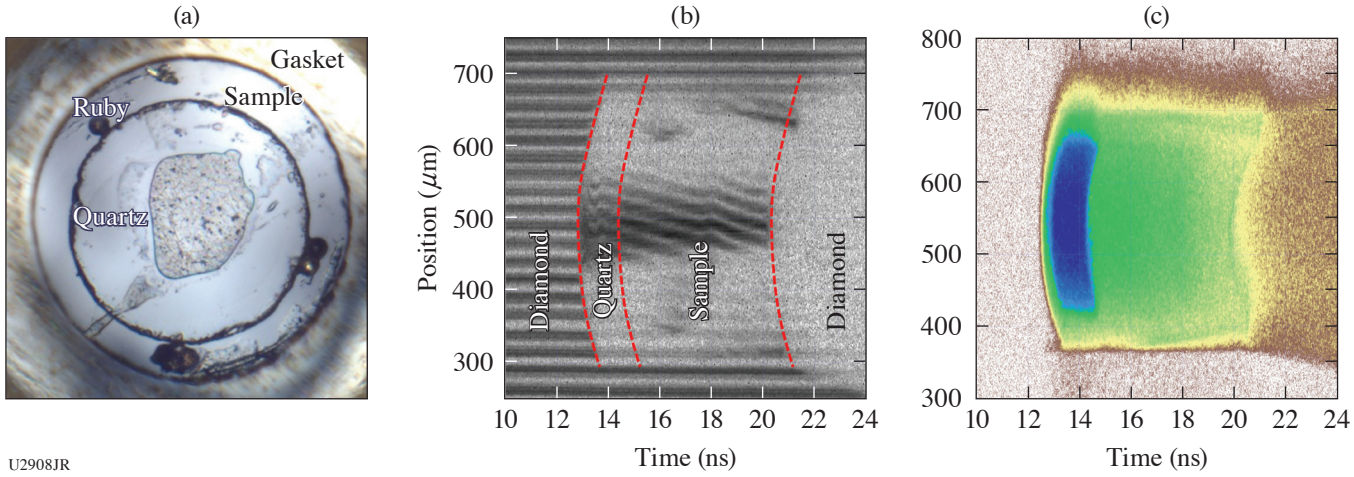

Figure 5
(a) Sample image. Example of (b) VISAR and (c) SOP data showing the decaying shock along the 100-mm-thick SU mixture on OMEGA.

This work was prepared by LLNL under Contract Number DE-AC52-07NA27344 and was supported by LLNL LDRD Program No. 19-ERD-031.

Particle Acceleration from Magnetically Driven Collisionless Reconnection Using Short-Pulse, Laser-Powered Capacitor Coils

L. Gao,[1*] S. Zhang,[2] A. Chien,[2] H. Ji,[1,2] E. G. Blackman,[3] and P. M. Nilson[4]
[1]Princeton Plasma Physics Laboratory
[2]Princeton University
[3]Department of Physics and Astronomy, University of Rochester
[4]Laboratory for Laser Energetics, University of Rochester
[*]Principal Investigator

Magnetic reconnection is a ubiquitous astrophysical process whereby magnetic energy is rapidly converted into plasma kinetic energy in the form of bulk flow, thermal energy, and nonthermal particles. The latter is often regarded as an observational signature of reconnection, which can be a more-efficient particle accelerator than other processes such as collisionless shocks. In the past ∼six years, our team has developed a platform to study acceleration of nonthermal electrons from magnetic reconnection at low plasma beta using UV laser-powered capacitor coils.[7] For the first time, nonthermal electrons accelerated by the reconnection electric field have been measured.[8] In our previous LBS campaigns, we have measured ultrastrong magnetic fields using short-pulse, laser-powered capacitor coils. The measured magnetic fields driven by the short-pulse lasers are ∼2 to 3× larger than those with UV lasers. In this new FY22 LBS shot day, we extended our platform to study particle acceleration by magnetically driven axisymmetric reconnection using short-pulse, laser-powered capacitor coils.

The experimental platform is shown in Fig. 6. The main target was composed of two Cu plates with an extended wing in the back plate, connected by a pair of parallel U-shaped coils. The OMEGA EP sidelighter (SL) was focused onto the wing section of the backplate, positively charging it up. The resulting voltage difference between the back and front plate drives currents in both coils for reconnection. Ultrafast protons generated by the backlighter (BL) probed through the coils to measure the magnetic-field distributions around the coils. The primary advantages of this target design were to (1) perform face-on proton radiography of the reconnection region, and (2) position multiple particle spectrometers around the coils to capture particles at various angles with respect to the reconnection region. The proton data, however, show very small magnetic-field generation for the new target. As a reference, our single-coil experiment used a capacitor coil target without the tiny wing and the SL was directly focused onto the back plate.

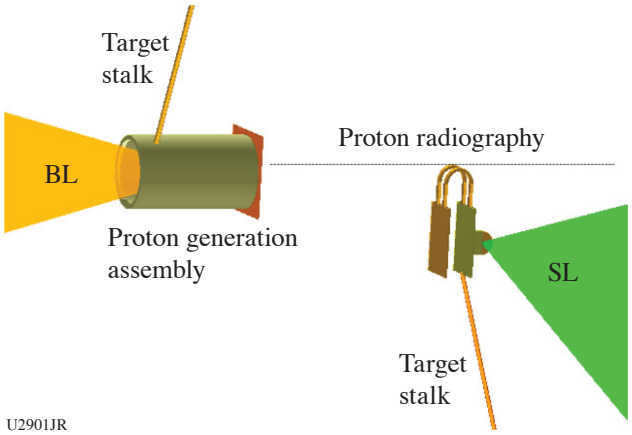

Figure 6
Experimental setup. The OMEGA EP SL was focused onto the wing section of the back plate, positively charging it up. The resulting voltage difference between the back and front plate drives currents in both coils, creating reconnection. Ultrafast protons generated by the BL probed through the coils and were collected by the proton film pack.

Two shots were dedicated to exploring magnetic-field evolution using the old single-coil target, where the SL was focused onto the back Cu plate. Figure 7 shows the proton images collected at 1 ns and 25 ps after the SL drive was turned off. Large and well-defined voids are observed for both cases, indicating a slow decay time of the coil current.

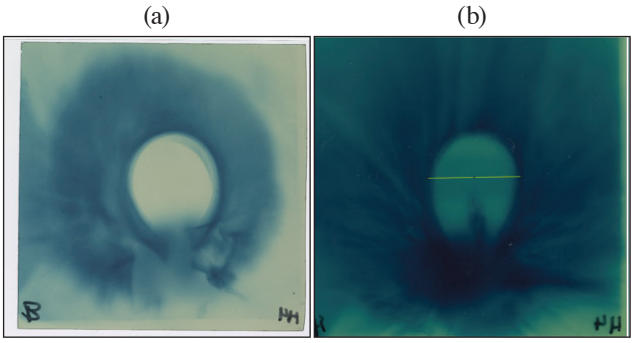

Figure 7
Proton radiographs of the single wire case at (a) 1 ns and (b) 25 ps, respectively, after the SL was turned off. The slight bubble is caused by magnetic fields around the wire deflecting incident protons.

In parallel to the LBS shot day, we conducted two LaserNetUS campaigns using the short-pulse, laser-powered coils for reconnection. Although the new target design with the tiny wing on the back plate did not work out, the data collected on this LBS day helped us with experiment designs for the two LaserNetUS campaigns where successful particle spectra were measured.

We acknowledge the Omega Laser Facility staff at the Laboratory for Laser Energetics. This work was performed under the auspices of U.S. DOE NNSA under the LBS Program, and the DOE Office of Science under the HEDLP Program No. DE-SC0020103.

Initial Relativistically Transparent Microchannel Experiments on OMEGA EP

H. G. Rinderknecht,* G. Bruhaug, M. VanDusen-Gross, and K. Weichman
Laboratory for Laser Energetics, University of Rochester
*Principal Investigator

In relativistically transparent interactions of high-intensity lasers with an overdense plasma, the ponderomotive force of the laser pulse is predicted to drive relativistic current filaments, which in turn produce an azimuthal magnetic filament strong enough to trap electrons.[9] The trapped electrons are predicted to be rapidly accelerated by direct laser acceleration (DLA) to high energies. In this campaign we studied magnetic filament acceleration using the OMEGA EP laser interacting with microchannel targets. The targets were arrays of 6-μm-ID microchannels filled with low-density CH foam, as shown in Figs. 8(a) and 8(b). From prior experiments and scaling laws,[10] we predicted that targets with lower density (3 mg/cm^3) would accelerate electrons more efficiently than targets with higher density (5 mg/cm^3); empty channel targets were also shot as a control.

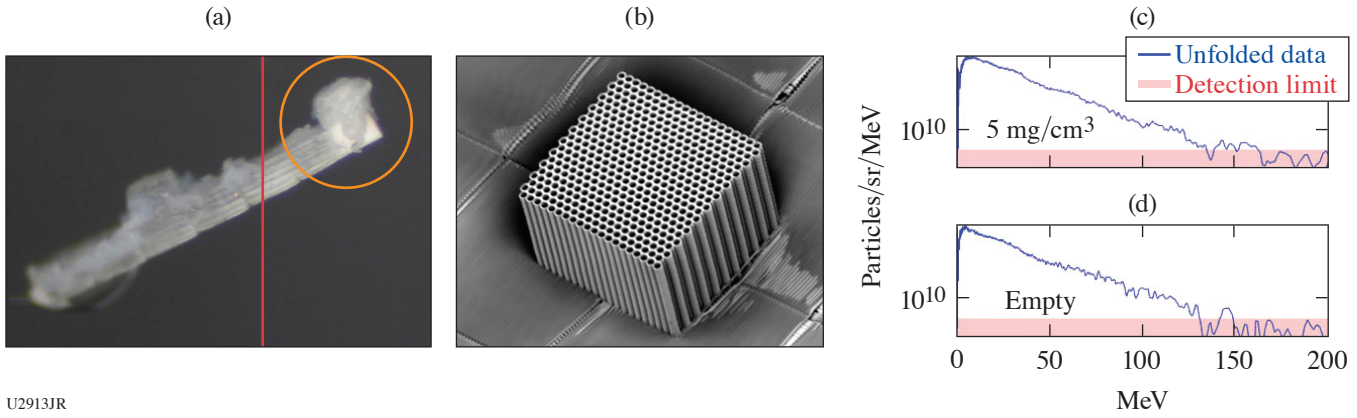

Figure 8
(a) Targets used in the experiment. The active component (orange) is an array of 6-μm-ID, 200-μm-long microchannels, either empty or filled with 3 mg/cm^3 or 5 mg/cm^3 CH foam. (b) Electron microscope image of an empty microchannel array. (c) Recorded electron spectrum from channels with 5-mg/cm^3 fill; (d) no fill. Recorded electron spectra were comparable for all target types.

The EPPS spectrometer recorded electron acceleration from all target types [Figs. 8(c) and 8(d)]. While both the fluence of electrons F and the average electron energy $\langle E\rangle$ increased significantly with higher peak laser amplitude $a_0\left(F \propto a_0^3,\ \langle E\rangle \propto a_0\right)$, no clear difference was observed between the three types of targets used. X-ray data recorded with the bremsstrahlung MeV x-ray spectrometer (BMXS) also did not show a significant difference in radiation between target types.

Post-shot 3-D particle-in-cell (PIC) simulations indicate that, for laser–channel interactions on the time scale of OMEGA EP, the initial channel fill is blown out of the channel within the first 300 fs of the interaction. Subsequently, plasma pulled from the channel wall fills the channels to a density of roughly 7× the plasma critical density in all cases, resulting in identical magnetic filament formation and electron acceleration in all cases. This supports the data interpretation that, on the time scale of OMEGA EP interactions, the magnetic filament acceleration is observed; however, initial plasma density does not determine the acceleration performance.

This material is based upon work supported by the DOE NNSA under Award Number DE-NA0003856, the University of Rochester, and the New York State Energy Research and Development Authority.

Inertial Confinement Fusion Plasma-Based Measurements of the T + ^{4}He Cross Section

J. Jeet,[1*] A. B. Zylstra,[1*] M. Rubery,[1] Y. Kim,[2] Z. L. Mohamed,[2] M. Gatu Johnson,[3] C. J. Forrest,[4] and V. Yu. Glebov[4]
[1]Lawrence Livermore National Laboratory
[2]Los Alamos National Laboratory
[3]Plasma Science and Fusion Center, Massachusetts Institute of Technology
[4]Laboratory for Laser Energetics, University of Rochester
[*]Principal Investigators

Inertial confinement fusion (ICF) implosions provide a relatively new platform for studying nuclear astrophysics. Unlike beam-target accelerator measurements, nuclear reactions occurring in these implosion experiments are a direct surrogate for astrophysical systems since the reactions occur at comparable plasma conditions. The tritium (T) + ^{4}He reaction is important for big-bang nucleosynthesis (BBN) production of ^{7}Li, which has a notable abundance anomaly. Observations of metal-poor halo stars[11] show approximately one-third of the ^{7}Li abundance from predictions that match the abundance inferred from the cosmic microwave background.[12] The important energy range for BBN is a center of mass energy (E_{CM}) between 60 and 160 keV (Ref. 13), corresponding to a range in temperature of 13 to 50 keV. The lower end of this range can be easily studied with implosions conducted at ICF facilities. The T + ^{4}He reaction produces ^{7}Li and a 2.4-MeV gamma, the latter of which can be measured using gamma detectors based on the Cherenkov mechanism. The gas Cherenkov detector (GCD-1) with a fused-silica radiator as well as the vacuum Cherenkov detector (VCD) are used to measure the gammas from this reaction. The implosions use all 60 of the OMEGA beams at 500 J per beam and a 1-ns square

pulse width. The capsules are 1-mm-diam, ~3-μm-thick Hoppe glass. The target fills consist of T + ^{4}He, as well as T_2 for a baseline comparison. Additionally, DT implosions are conducted along with a carbon puck attached to GCD-1 to calibrate both GCD-1 as well as the VCD.[14] Figure 9(a) shows the results of the calibration of the detector response, for both the GCD-1 and the VCD, to 4.4-MeV carbon gammas resulting from inelastic scattering of DT neutrons with the carbon puck. Figure 9(b) shows the gamma measurements made by GCD-1. These are average signals from multiple shots for each fuel type normalized to both the DT and TT neutron yields. The DT and TT yield-normalized signals measured for the T^{4}He fills (black solid and blue solid curves, respectively) are consistent and within 10%. These are significantly larger than the background measurements provided by the T_2 gas fills (dashed curves).

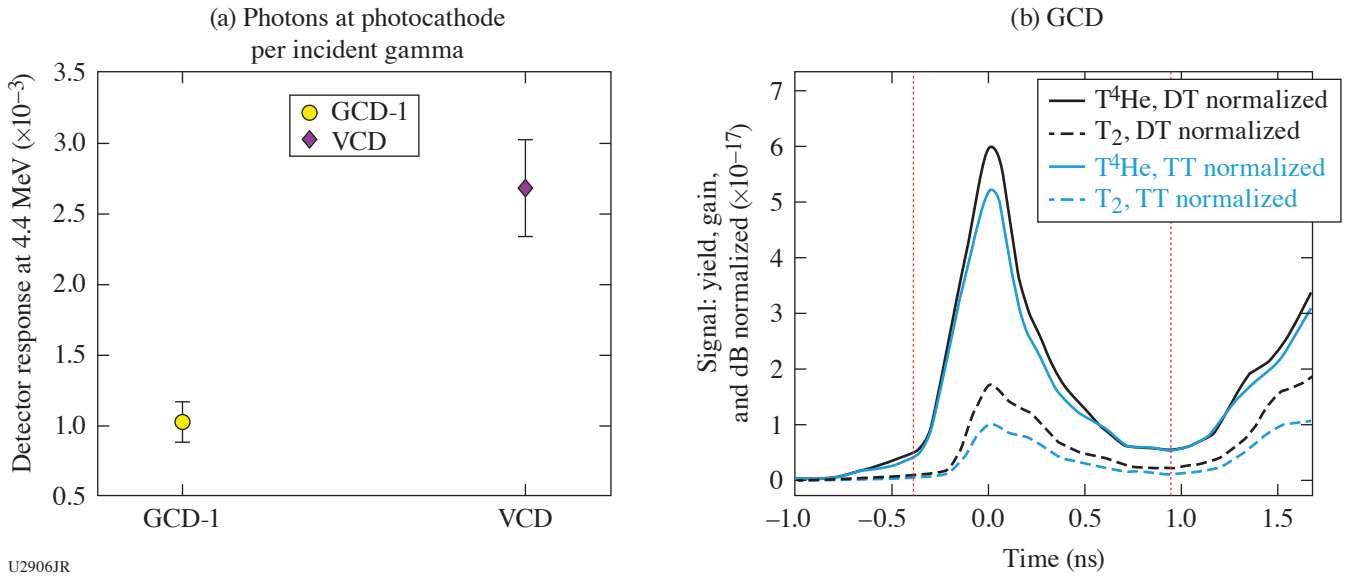

Figure 9
(a) The detector response, for both the GCD-1 with a fused-silica radiator as well as the VCD, is measured to 4.4-MeV gammas, resulting from inelastic scattering of DT neutrons with a carbon puck attached to the GCD-1. (b) Average gamma signals as measured by GCD-1 are shown for each fuel type, T^{4}He (solid) and T_2 (dashed), and normalized to the DT (black) and TT (blue) neutron yields. The excess gamma signal in the T + ^{4}He reaction relative to the T_2 gas fills, for each type of yield normalization, agree with one another within a factor of 10%.

The excess gamma signal, along with the detector calibrations, will be used to determine *S* factor for the T + ^{4}He reaction. The results of these experiments can potentially impact the BBN modeling community by improving confidence in the reaction rate at relevant energies.

We thank the operations crews and engineering staff at Omega for supporting these experiments. This work was performed under the auspices of the U.S. Department of Energy by Lawrence Livermore National Laboratory in part under Contract No. DE-AC52-07NA27344 and supported by the U.S. DOE Early Career Research Program (Fusion Energy Sciences) under FWP SCW1658.

X-Ray Sources from Laser Wakefield Acceleration on OMEGA EP

F. Albert,[1*] I. Pagano,[1,2] N. Lemos,[1] J. Williams,[1] H. Chen,[1] J. L. Shaw,[3] D. H. Froula,[3] C. Arrowsmith,[4] A. Aghedo,[5] M. Sinclair,[6] and C. Joshi[6]
[1]Lawrence Livermore National Laboratory
[2]University of Texas, Austin
[3]Laboratory for Laser Energetics, University of Rochester
[4]University of Oxford, UK
[5]Florida A&M University
[6]University of California, Los Angeles
*Principal Investigator

X-ray backlighting is one of the most used methods to look into the extreme temperatures, pressures, and densities created during laser-driven high-energy-density science (HEDS) experiments. Over the years, much effort has gone into developing backlighting techniques to look into these states of matter, with new sources and diagnostics. The properties of an x-ray backlighter (flux, source size, spectrum, duration) required for an experiment depend on the application being studied and on the quantity being measured. The goal of the Wakefield-EP shot series is to develop a new type of x-ray backlighter, which could be advantageous for applications requiring broadband spectra, small source sizes (sub-50 μm), short duration (less than 10 ps), and x rays extending beyond 100 keV. Our proposed x-ray sources are based on laser wakefield acceleration (LWFA) of electrons in the self-modulated regime (SMLWFA). Specifically, we aim to develop three different x-ray sources based on betatron radiation, Compton scattering, and bremsstrahlung emission.

The WakefieldLBS-EP-22A shot day was a continuation of our previous work, aimed at producing and detecting x-ray radiation produced by SMLWFA using a modified version of the EPPS diagnostic. We enlarged apertures to 5 mm (instead of 1 mm) and included a hole at the back of the magnet box, as well as a stack of nine image plates at the back of the ten-inch manipulator (TIM) boat to detect betatron radiation. In addition to betatron radiation, this year we also measured x rays produced by inverse Compton scattering, where the OMEGA EP laser pulse was reflected by a foil onto the accelerated electrons to produce high-energy x rays. We also implemented a new crosshair on the front end of the EPPS diagnostic to be able to measure the x-ray source size. The wakefield platform continued to produce robust electron beam data, recording a >100-nC charge electron beam at each shot, as well as two temperature spectra extending up to about 200 MeV (see Fig. 10).

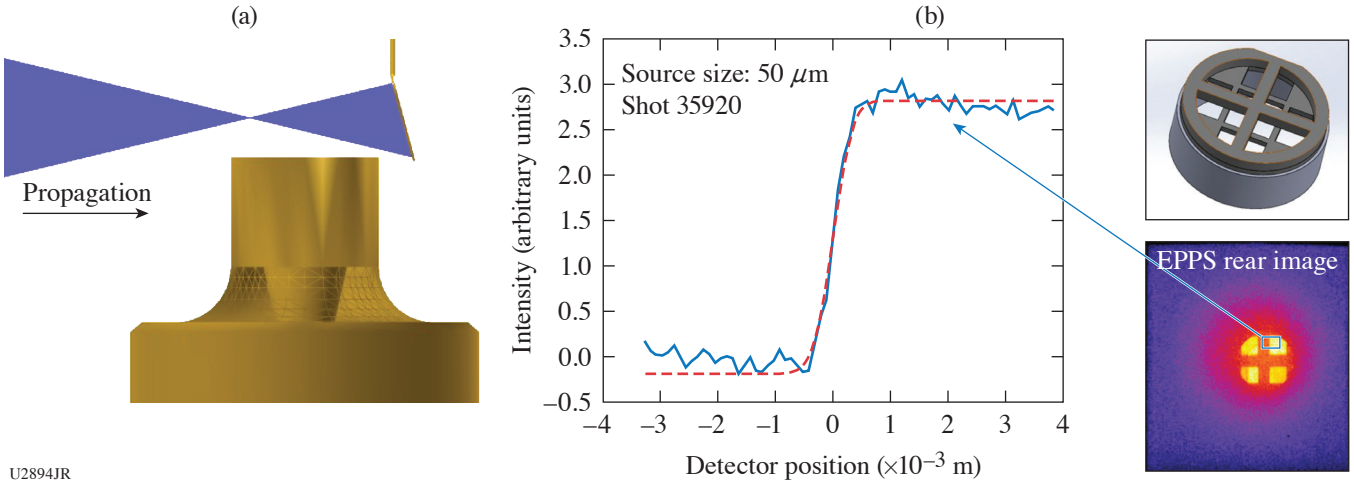

Figure 10
Results obtained during the WakefieldLBS-EP-22A shot day using the modified EPPS diagnostic. (a) Setup for an inverse Compton scattering x-ray source; (b) x-ray source size measurement and analysis.

Extreme THz Generation and Detection

G. Bruhaug,[1*] H. G. Rinderknecht,[1] Y. E,[2] M. S. Wei,[1] K. G. Francis,[2] X. C. Zhang,[2] G. W. Collins,[1] and J. R. Rygg[1]
[1]Laboratory for Laser Energetics, University of Rochester
[2]The Institute of Optics, University of Rochester
[*]Principal Investigator

For several decades, the creation of THz radiation was considered extremely challenging due to the frequency in question being too fast for classic electronic switching techniques and not efficiently generated via classic optical sources.[15] The first usable THz sources were based on large particle accelerators and were created via either synchrotron radiation or as free-electron lasers.[15,16] Later source development led to the creation of laser-based sources utilizing nonlinear crystals for frequency conversion.[15–18] Commercial laser-based sources of THz radiation are now widely available and utilized for homeland security applications, medical imaging, and traditional materials science research. However, these laser-based sources are limited in average and

peak THz power by the damage limits of nonlinear crystals.[15–18] This limits their applications in noisy environments and as drivers for pump–probe experiments. Newer laser-plasma–based THz sources have been developed using high-intensity lasers (>10^{18} W/cm^2) and have shown great promise as both experimental pumps and probes.[15,18] These THz generation methods involve irradiating foils, wires, and gas jets with high-intensity lasers.[15–20]

We performed the first laser-plasma THz generation experiments on OMEGA EP that tested our new THz background/energy meter (TBEM) detectors and showed extremely high THz yield from foil targets, similar to previous experiments on smaller lasers.[15] Analysis is still ongoing, but we estimate hundreds of mJ of THz were made from laser energies ranging up to 200 J. In addition, we performed the first ever attempts at THz/proton interferometry using TNSA protons. This measurement utilized OMEGA EP's unique dual-axis short-pulse capability and performed the first ever proton measurements of extreme THz fields, but not at the same time as the TBEM detectors due to background noise issues that have now been resolved in the detector design. A typical TNSA "proton tube" target was driven with a 10-ps, 900-J laser pulse and then ~90 ps later a THz generating foil was driven with a 0.7-fs, 500-J laser [Fig. 11(a)]. Both targets were positioned 5 mm from target chamber center, keeping each target out of the sheath field region of the resulting plasmas.

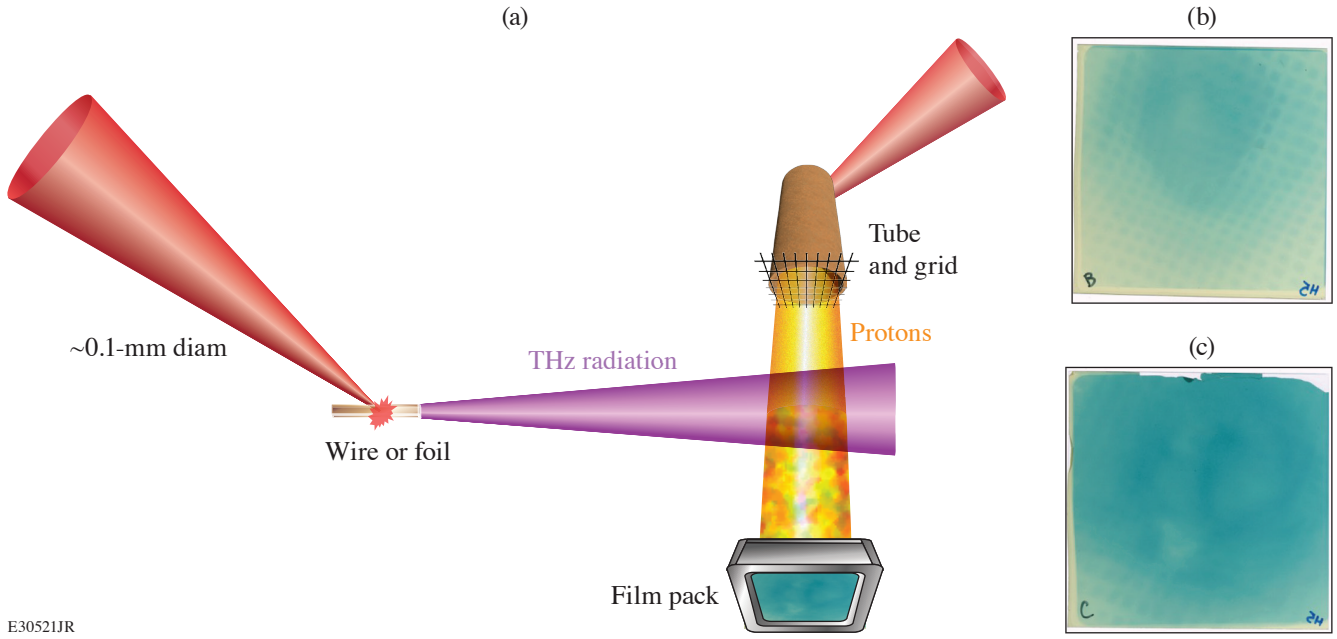

Figure 11
(a) Outline of the THz/proton interferometry experimental setup; (b) 15-MeV proton radiograph without any THz radiation present; and (c) 15-MeV proton radiograph with a THz pulse incident on the protons.

The THz pulse is believed to be single or even half-cycle, which allows the large (GV/m) electric fields in the pulse to provide net momentum to the protons. A test shot was taken [Fig. 11(b)] without a THz foil and a typical TNSA proton source is seen. The addition of a THz pulse altered the proton radiographs [Fig. 11(c)] in energies ranging from 10 to 28 MeV. These phenomena were repeatable between shots and became weaker with a lower-energy laser driver, as would be expected. Analysis is still ongoing but we believe GV/m electric fields generated this effect, requiring >100-mJ THz pulses. We anticipate that further analysis will allow exact discernment of the THz pulse energy and field strength, as well as provide a rough estimate as to the spectral distribution. The TBEM research and development performed during these experiments were also crucial for finalizing detector design and allowing for the detection of even higher THz yields on later OMEGA EP experiments.

This material is based upon work supported by the Department of Energy National Nuclear Security Administration under Award Number DE-NA0003856, the University of Rochester, and the New York State Energy Research and Development Authority.

Quantum States of Hydrogen: Toward a Superconducting Superfluid

A. Schwemmlein,[1*] G. W. Collins,[1*] R. Jeanloz,[2] S. Brygoo,[3] P. M. Celliers,[4] J. H. Eggert,[4] D. E. Fratanduono,[4] R. Hemley,[5] P. Loubeyre,[3] M. Millot,[4] J. R. Rygg,[1] Y. Kim,[4] J. Sater,[4] L. E. Hansen,[1] Z. K. Sprowal,[1] and R. Earley[1]
[1]Laboratory for Laser Energetics, University of Rochester
[2]University of California, Berkeley
[3]Commissariat à l'énergie atomique et aux énergies alternatives, France
[4]Lawrence Livermore National Laboratory
[5]University of Illinois, Chicago
[*]Principal Investigators

Crystalline metallic hydrogen has attracted significant theoretical interest since the 1930s (Ref. 21). Recent theoretical work suggests that its quantum nature gives rise to remarkable properties like high-temperature superconductivity.[22] In addition, metallic hydrogen is the predominant constituent of giant planets and stars; it is thus the most abundant form of condensed matter in the universe. Experimental studies of crystalline metallic hydrogen, however, have only recently become possible using dynamic-compression experiments at high-intensity laser facilities like Omega.

To reach the necessary low temperatures (<1000 K) and high pressures (>500 GPa), a low-temperature and entropy initial state is compressed using a custom OMEGA pulse shape approximating an isentropic drive. To reduce the entropy of the targets, only hydrogen molecules in the low-entropy solid and parastate, where the proton spins not aligned, are used. This special state of hydrogen was successfully produced in a newly developed target fill and diagnostic station, which confirmed >95% purity and stability of this state over hours in the standard planar cryo targets. These targets were cooled down in the target chamber to 10 K while observing the formation of a uniform solid using the VISAR field of view.

Raw data with a preliminary analysis of a representative shot is shown in Fig. 12. The VISAR fringes (background) were converted into the pusher velocity (green) that was subsequently matched using a hydrocode, which finally revealed a maximum

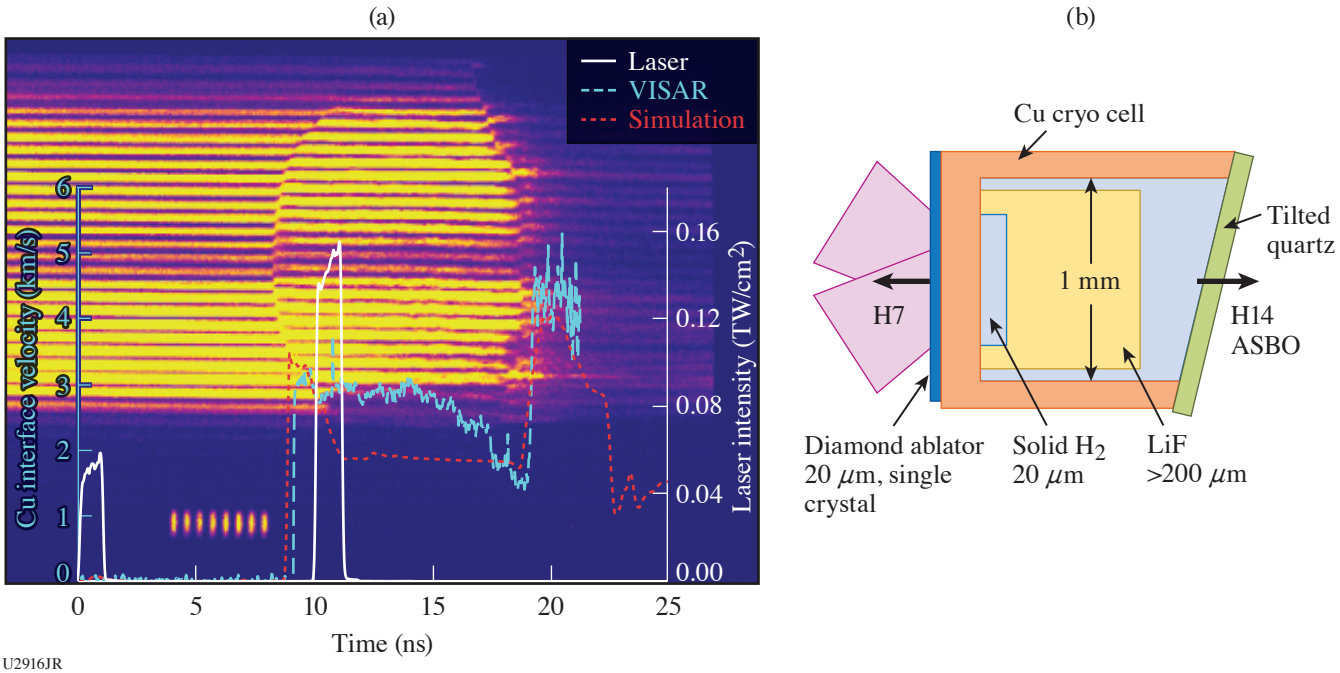

Figure 12
(a) VISAR raw data and analysis of (b) a 10-K parahydrogen target shot by a two pulse sequence. The VISAR sees the copper pusher in front of the 20-μm-thick hydrogen payload. The simulation revealed that a maximum pressure of 40 GPa was reached. Future experiments will use these two pulses in combination with a 12-ns ramp.

pressure of 40 GPa inside the 20-μm hydrogen payload. For this experiment, the first two pulses of a six-pulse sequence that was optimized using a hydrocode were tested. These two 1-ns square pulses initiate the ablation and reverberate inside the hydrogen to increase the pressure to several tens of GPa. A subsequent 12-ns ramp will be added in future experiments to increase the pressure to 700 GPa at a temperature around 1000 K. Simulations using the standard code *HYADES* indicate that these conditions can be met.

This experiment was conducted at the Omega Laser Facility at the University of Rochester's Laboratory for Laser Energetics with the beam time through the Laboratory Basic Science program.

Viscosity Measurements Using Tracer Particles

A. Gleason,[1*] J. Shang,[2,3] D. N. Polsin,[2,3] H. Aluie,[2,3] and J. R. Rygg[2,3]
[1]SLAC National Accelerator Laboratory, Stanford University
[2]Department of Mechanical Engineering, University of Rochester
[3]Laboratory for Laser Energetics, University of Rochester
[*]Principal Investigator

Any study of hydrodynamic flows in HED environments requires knowledge of material properties such as dynamic viscosity, and its inclusion in simulations can dramatically alter flows such as in inertial confinement fusion implosions.[23] Measurements of viscosity under HED conditions are sparse. In this campaign, we collected additional data to quantify the viscosity of epoxy, a surrogate for polystyrene and other commonly used ablator materials, to corroborate against a previous campaign. The method relies on measuring the acceleration of bluff bodies embedded in the material of interest since the hydrodynamic forces include viscous contributions; the viscosity can be estimated from the trajectory.[24]

In the experiment, the epoxy was embedded with titanium microspheres. The target was then shock compressed to ~215 GPa and we imaged the backlit target at different times after the shock had traversed the spheres. Figure 13 shows images of the instantaneous particle position and compression of two Ti spheres entrained in the flow behind the shock, and their displacement from their pre-shock location. Due to the lower mass of the spheres compared to the last experiment, we expect that our analysis will show they accelerate faster than the spheres in our last campaign.

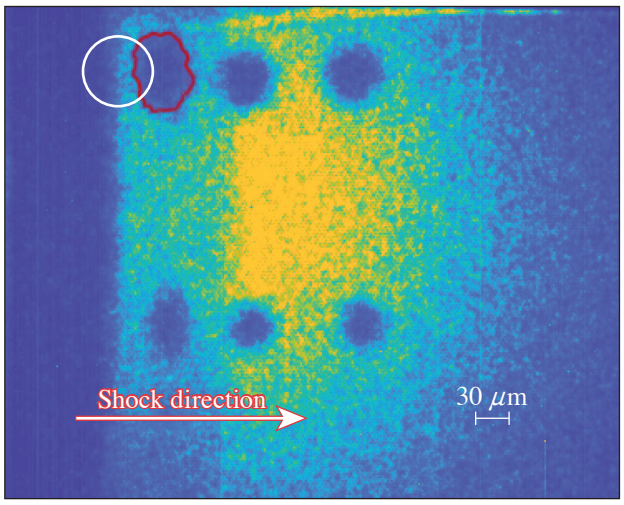

U2903JR

Figure 13
Radiograph of shocked and unshocked titanium particles for shot 105537 at t = 19.7 ns after the drive. The initial location of the larger sphere is outlined in white; the instantaneous particle position is shown in red, showing a displacement of about 40 μm after acceleration. Spheres are compressed behind the shock.

The experiment was conducted at the Omega Laser Facility at the University of Rochester's Laboratory for Laser Energetics with the beam time through the LBS Program. This work was supported by the DOE Office of Fusion Energy Sciences under the Early Career Award for A. Gleason. This work was also supported by US Department of Energy and NNSA under awards DE-SC0019329 and DE-NA0003914. Partial support from grants NSF PHY-2020249, DE-SC0020229 and DE-NA0003914 is also acknowledged.

Formation of Dynamic Shells Using Foam Ball Targets

I. V. Igumenshchev,[1*] W. Theobald,[1] C. Stoeckl,[1] R. C. Shah,[1] D. T. Bishel,[1] V. N. Goncharov,[1*] P. Adrian,[1] M. J. Bonino,[1] E. M. Campbell,[1] D. A. Chin,[1] T. J. B. Collins,[1] S. Fess,[1] D. R. Harding,[1] S. Sampat,[1] N. R. Shaffer,[1] A. Shvydky,[1] W. T. Trickey,[1] L. J. Waxer,[1] A. Colaïtis,[2] R. Loitard,[2] S. Atzeni,[3] F. Barbato,[3] and L. Savino[3]
[1]Laboratory for Laser Energetics, University of Rochester
[2]Centre Lasers Intenses et Applications, France
[3]University of Rome, Italy
[*]Principal Investigators

A dynamic-shell (DS) concept in direct-drive ICF utilizes the conventional hot-spot–ignition scheme and uses about 3-mm-diam sphere targets of liquid deuterium–tritium (DT) as a fuel.[25] Implosion shells of DT, which are required for hot-spot ignition, are developed dynamically from such sphere targets. This development and ignition are accomplished in four distinct evolution stages. In the first stage, a liquid DT sphere target is compressed by a few-Mbar convergent shock wave, which is launched by intense laser beams symmetrically irradiating the target. The second stage starts when this shock reaches the target center, reflects, and is transformed into a blast wave, causing the shock-compressed fuel, now becoming a plasma cloud, to expand. The third stage begins with launching convergent shocks at the outer edge of the expanding cloud. These shocks decelerate and reverse the expansion, resulting in a dynamic formation of a dense shell. In the fourth stage, this shell is imploded using a megajoule laser pulse similar to that in the conventional hot-spot–ignition scheme.

Proof-of-principle experiments on the OMEGA laser[26] have demonstrated, for the first time, the feasibility of DS formation and stability of DS's to low-mode perturbations (for Legendre modes less than about 10) using a scaled-down experimental setup to accommodate limitations in the available laser energy (<20 kJ) and pulse duration (<4 ns). The experiments used room-temperature surrogate sphere targets consisting of a CH foam and having an outer diameter of about 600 μm [see Fig. 14(a)]. Foam targets in the OMEGA experiments undergo the same evolution stages (compression, expansion, and shell formation) as in the ignition design, excluding the final implosion/ignition stage. Figure 14(b) illustrates these stages, showing a simulated shock diagram in gray scales for OMEGA shot 105251. The laser pulse is shown by a red line and has 11.2-kJ energy. The square pulse in the beginning of the pulse (see the red line) launches a shock that initially compresses the target. This shock reflects from the center at t = 1.4 ns, forming a blast wave and resulting in expansion of the compressed target mass. The second square pulse, which

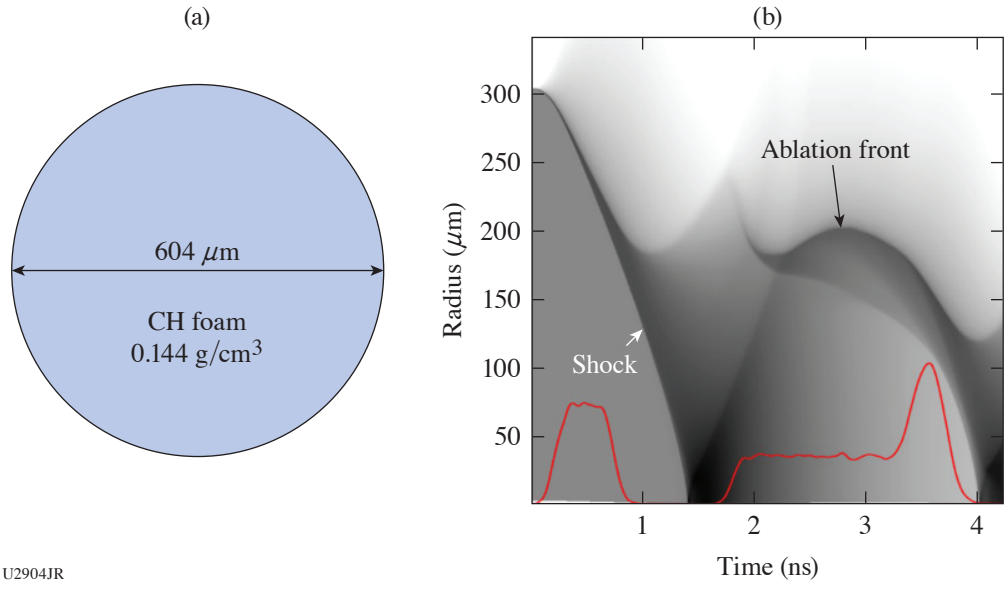

Figure 14
(a) Foam-ball target and (b) simulated log-density evolution, or "shock diagram," for OMEGA shot 105251. The red line in (b) shows the laser pulse in relative units.

starts at $t = 1.8$ ns, decelerates the expanding mass by sending convergent shocks and forms a dense shell. The outer shell radius, which is defined as the radius of the ablation front and seen as a density-contrast interface in Fig. 14(b), is initially reduced to about 180 μm at 2.15 ns, then increased, reaching about 200 μm at 2.8 ns, and then decreased again, approaching the minimum of about 120 μm at 4.0 ns [see Fig. 14(b)]. The power spike at the end of the pulse helps to additionally compress the shell mass, increasing the contrast in density at about 3.7 to 4 ns. This time interval is the most favorable for probing the formation of DS.

The experiments employed three x-ray diagnostics to evidence the DS formation. These include a streaked self-emission radiography,[27] backlighting radiography,[28] and framed shadowgraphy.[29] Figure 15(a) shows the streak data (the color map) aligned with the laser pulse (the white line) that were obtained in shot 105251. Two bright spots at $t \approx 1.4$ and 3.9 ns near $y = 0$ correspond to shock bounce events that were predicted in simulations [see Fig. 14(b)]. The bright region between $t \approx 1.9$ and 3.9 ns represents the emission at the ablation-front during the formation of DS. The rims bounding this region in the top and bottom show the ablation front trajectory. These data, while not directly indicating the formation of DS, make it possible to verify the simulations in Fig. 14(b), which show good quantitative agreements with inferred shock timing and ablation-front trajectory.

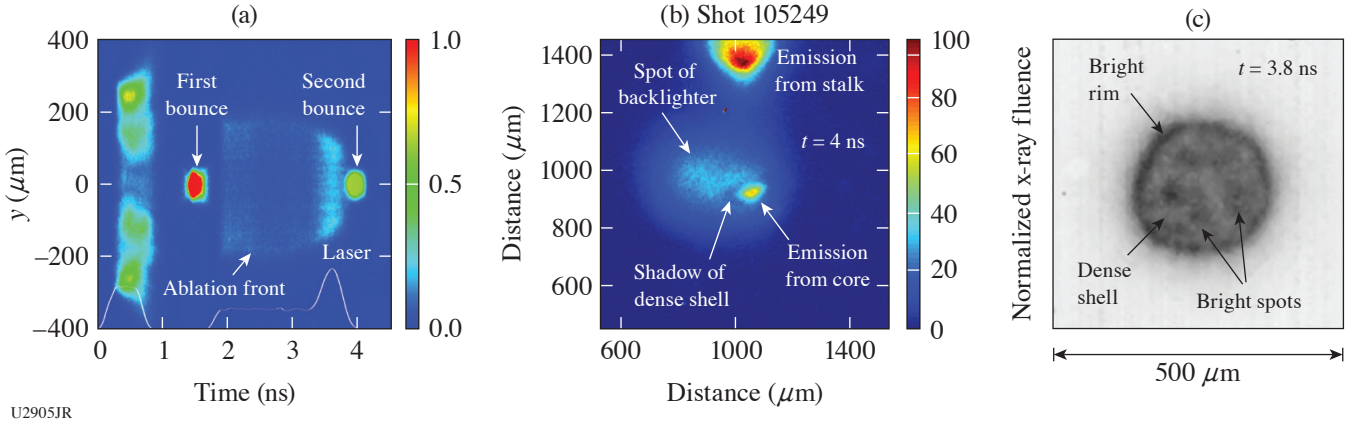

Figure 15
(a) X-ray streaked self-emission radiograph from shot 105251, (b) backlighting radiograph from shot 105249, and (c) framed shadowgraph from shot 105251.

Figure 15(b) illustrates results of backlighting radiography performed using joint OMEGA and OMEGA EP shot 105249. A 25-ps x-ray backlighter pulse (1.865 keV) was fired at $t \approx 4.0$ ns using the high-intensity OMEGA EP beam illuminating a Si foil target. This moment corresponds to the maximum convergence of DS, causing bright emission of the hot shell interior, or the core. The shadow on the background of backlighter and core emission is clearly visible in Fig. 15(b) and directly evidences the formation of a DS. Note the emission from remnants of a plastic (CH) stalk in the upper part of this figure. This stalk had a diameter of 50 μm and was used to mount the target. Its emission is observed far from the shell and without apparent influence of the formation of DS. This agrees with results of 3-D radiation-hydrodynamic simulations using the code *ASTER*,[30] which predict that the stalk is completely ablated off during earlier evolution (up to $t \approx 2$ ns) and does not significantly affect the shell dynamics.

The shadowgraph in Fig. 15(c) shows the DS at the late stage of its formation, $t \approx 3.8$ ns. The bright (dark in the image) circular rim in this figure corresponds to x-ray emission just outside the ablation front. The less-bright regions inside the rim represent the developed DS, which shadows x rays coming from the ablation front on the opposite side of the shell with respect to the viewing direction and from the hot shell interior. The five almost symmetric bright spots (again, darker in the image) inside the rim appear from perturbations in the shell coming from the OMEGA 60-beam illumination pattern. There are five of them because the viewing direction is projected through the center of a pentagon formed by the OMEGA beam ports. Three-dimensional *ASTER* simulations suggest that OMEGA beam overlapping can result in dips in the dense shell in the locations of maximum on-target intensity. This causes the emission from the shell interior to escape more efficiently through these dips resulting in imaging symmetric bright spots.

This material is based upon work supported by the Department of Energy National Nuclear Security Administration under Award Number DE-NA0003856 and ARPA-E BETHE Grant No. DE-FOA-0002212. The experiment was conducted at the Omega Laser Facility at the University of Rochester's Laboratory for Laser Energetics with the beam time through the Laboratory Basic Science program.

Inertial Confinement Fusion Plasma-Based Measurements of the D–T γ-to-Neutron and the D–^{3}He γ-to-Proton Branching Ratios

J. Jeet,[1*] A. B. Zylstra,[1] M. Rubery,[1] M. Eckart,[1] Y. Kim,[2] Z. L. Mohamed,[2] K. Meaney,[2] M. Gatu Johnson,[3] C. J. Forrest,[4] and V. Yu. Glebov[4]
[1]Lawrence Livermore National Laboratory
[2]Los Alamos National Laboratory
[3]Plasma Science and Fusion Center, Massachusetts Institute of Technology
[4]Laboratory for Laser Energetics, University of Rochester
[*]Principal Investigator

The D–T γ-to-neutron branching ratio [^{3}H(d,γ)^{5}He/^{3}H(d,n)^{4}He] has been previously determined in beam–target-based experiments as well as in ICF experiments.[31,32] In the latter case, neutron-induced backgrounds are significantly reduced compared to the former due to the short-pulse nature of ICF implosions and the use of gas Cherenkov γ-ray detectors. A benefit of ICF-based measurements is the ability to achieve lower center-of-mass energies as compared to accelerators. Previous ICF-based experiments, however, report a large uncertainty in the D–T γ-to-neutron branching ratio of ≈48%. A more-precise value for the branching ratio based on data taken at OMEGA has been determined. This relies on a cross-calibration against the better known ^{12}C neutron inelastic scattering cross section [^{12}C(n,n′)γ] in a puck-based experiment involving the gas Cherenkov detector (GCD-3). A D–T branching ratio value of $(4.6\pm0.6) \times 10^{-5}$ is determined by this method;[33] the results are shown in Fig. 16 and compared to values obtained in previous experiments. This campaign will improve this experiment to further reduce the uncertainty in the measurement. We will also provide a measurement of the D–^{3}He γ-to-proton branching ratio to significantly better precision than reported by previous experiments, which are limited to ≈33%. This is made possible due to an absolute detector calibration that relies on the inelastic scattering of DT neutrons in a carbon puck attached to the GCD-3 (Ref. 14). The resulting 4.4-MeV gammas are temporally separated from the primary gamma signal resulting from the D–T fusion and can be isolated by performing a yield-normalized subtraction of a background signal that does not field the carbon puck. Signals as measured by the VCD are shown in Fig. 17 for the D–T implosions.

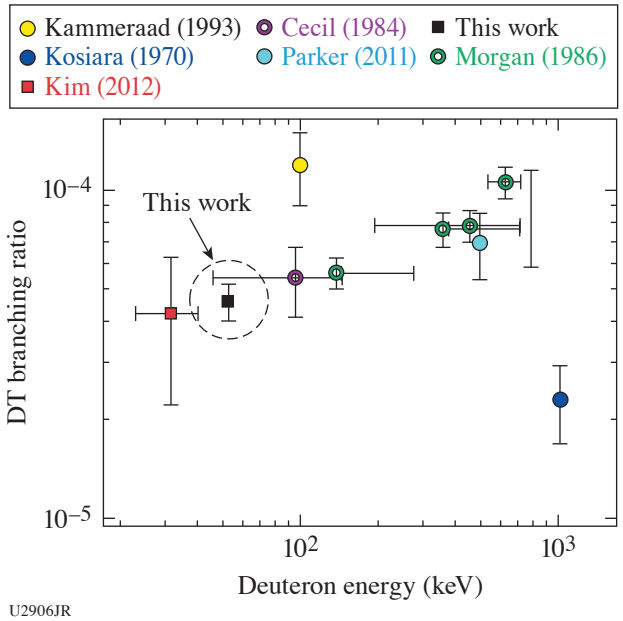

Figure 16
The D–T branching ratio measurement resulting from the work of Ref. 33 is shown (black square) along with other recent experiments (Refs. 31 and 32), which include both beam–target-based measurements (dark blue circle) as well as an ICF-based result (red square).

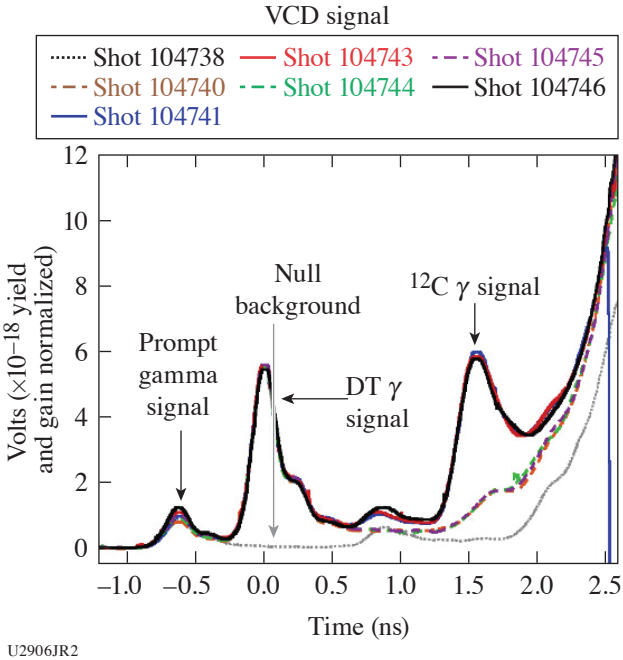

Figure 17
D–T implosion signals as measured by the VCD. Each signal is comprised of different features. The prompt gamma signal results from direct interaction of gammas with the photomultiplier tube inside the VCD. The DT gamma signal results from the fusion and is delayed with respect to the prompt gamma signal. The ^{12}C gamma signal results from the inelastic scattering of DT neutrons with a carbon puck attached to the GCD-3. The resulting 4.4-MeV gammas are temporally separated from the primary D–T fusion gammas.

Relative to the experimental data analyzed in Ref. 33, these experiments were optimized to improve the precision in the measurement. The TIM diagnostic loadout is kept minimal to reduce the extraneous neutron-induced noise that can coincide with the ^{12}C gamma signal. A thinner capsule shell is used to minimize shell areal-density contributions to the primary D–T fusion gamma signal. Measurements were taken with multiple gamma detectors, GCD-3 as well as the VCD, at different threshold energies. The ratio of the ^{12}C gamma signal to that of the DT gamma signal allows for extraction of the D–T branching ratio while eliminating the need for absolute detector calibrations and systematic yield uncertainties for the measured DT neutrons. D^{3}He shots were also conducted in this campaign to determine the gamma-to-proton branching ratio, which is measured to higher precision using the absolute detector calibration provided by the ^{12}C gamma measurement.

With improved measurements of the ^{12}C(n,n′)γ scattering cross section or the D–T γ spectrum, the data taken in this campaign can be revisited and systematic uncertainties in the D–T γ-to-neutron and D–^{3}He γ-to-proton branching ratios can be further reduced.

We thank the operations crews and engineering staff at Omega for supporting these experiments. This work was performed under the auspices of the U.S. Department of Energy by Lawrence Livermore National Laboratory in part under Contract No. DE-AC52-07NA27344 and supported by the U.S. DOE Early Career Research Program (Fusion Energy Sciences) under FWP SCW1658.

Detailed Benchmarking of the Nernst Effect in a Magnetized High-Energy-Density Plasma

S. Malko,[1*] W. Fox,[1,2] D. B. Schaeffer,[2] C. Walsh,[3] G. Fiksel,[4] A. J. Harvey-Thompson,[5] M. Weiss,[5] A. Hansen,[5] D. Ruiz,[5] A. Bose,[6] C. Frank,[6] P. Heuer,[7] and J. Davies[7]

[1]Princeton Plasma Physics Laboratory
[2]Princeton University
[3]Lawrence Livermore National Laboratory
[4]Center for Ultrafast Optical Science, University of Michigan
[5]Sandia National Laboratories
[6]University of Delaware
[7]Laboratory for Laser Energetics, U. Rochester
[*]Principal Investigator

Magnetic fields are known to affect and suppress heat flux through thermomagnetic effects in HED laser-produced plasmas.[34] In the high-beta and moderate collisionality regimes on HED plasmas, however, the heat flux can also feedback and drive advection of the magnetic field via the Nernst effect. This can be important for several applications of magnetized HED plasmas, including magnetized liner inertial fusion (MagLIF).[35] The heating laser creates a radial temperature and density gradient in the D_2 fuel perpendicular to the axial magnetic field. Simulations show that the Nernst effect significantly reduces the performance of the MagLIF preheat phase by advecting the applied axial magnetic field out of the fuel, thereby increasing energy losses due to thermal conduction.[36] Nernst transport can also strongly affect the dynamics of both externally applied and self-generated magnetic fields in hohlraums and ablation fronts in directly driven capsules in ICF and ICF hot spots. The detailed experimental benchmarking of numerical models that include the Nernst effect are crucial and required to further understand how to control such magnetized plasma systems. To identify the importance of this effect, one can introduce the "Nernst number" N_e, which gives the ratio of the characteristic velocity of the Nernst field advection v_N to the sonic plasma expansion v_s, $N_e = v_N/v_s$.

Here we report on novel experimental platform NerntEffect22A at the Omega Laser Facility for benchmark Nernst effect in the regime where the Nernst advection dominates the frozen-in plasma flow $0.1 < N_e < 1$. The platform is based on laser heating of a gas jet in a magnetic field and simultaneous direct measurement of the Nernst velocity and plasma conditions (density and temperature). In order to design this experiment and find the regime of interest, we performed a pre-shot parametric study with 1-D *GORGON*[37] by varying gas densities, gas type, laser energy, and magnetic field. In addition, *FLUKA*[38] Monte Carlo simulations were used to obtain expected proton signal level and design proton radiography diagnostics.

The setup of experiment is presented at Fig. 18. One OMEGA beam (heater) with 500-J energy is used to heat a H_2 gas jet in a cylindrically symmetric volume aligned parallel to an external magnetic field of approximately 5 T produced by MIFEDS. Proton radiography with 3- and 15-MeV monoenergetic protons produced from a D–^{3}He implosion was used to measure the magnetic fields at several expansion times. The plasma parameters (n_e, T_e) and radial bulk flow speed of plasma at different positions across cavity (0, +250 μm, +500 μm) were measured by time-resolved 2ω optical Thompson scattering (OTS).

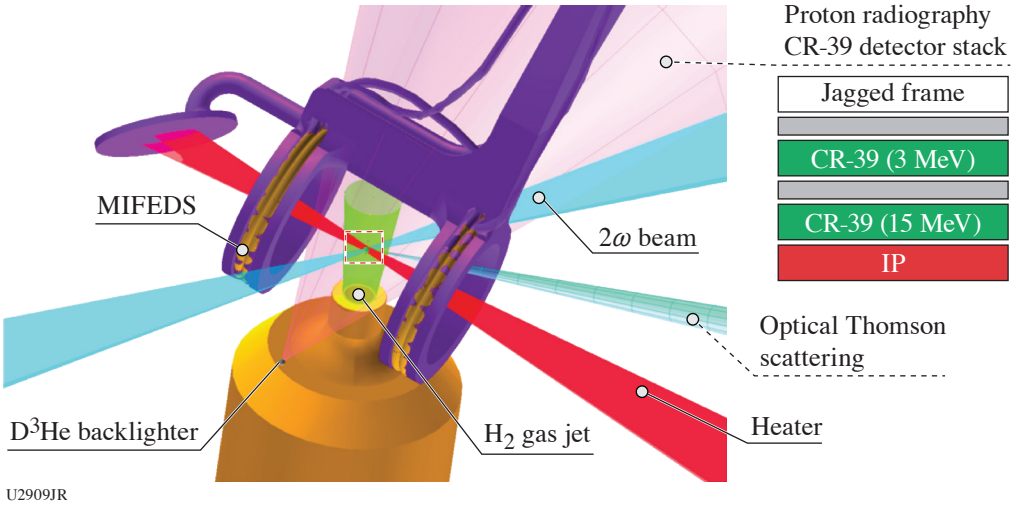

Figure 18
The experimental setup at the Omega Laser Facility. IP: image plate.

The example of obtained proton radiography data at 0.5- and 1-ns expansion time is shown in Fig. 19. We have observed a clear magnetic-field cavitation and pileup on the edges of the cavity as predicted by 1-D *GORGON* simulations. The measured time evolution of the cavity will allow us to calculate the cavitation rate and thus the Nernst velocity. The preliminary analysis of OTS electron plasmon wave (EPW) and ion-acoustic wave (IAW) spectra at the center of cavity provided electron temperature of $T_e \sim 400$ eV and electron density of 1×10^{20} cm^{-3} at 700-ps expansion time. Based on these measurements we have estimated $N_e \sim 0.28$ compared to 0.12 for the MagLIF preheat phase.[39] These experimental results will be compared with *GORGON*, *HYDRA*, and *LILAC* simulations.

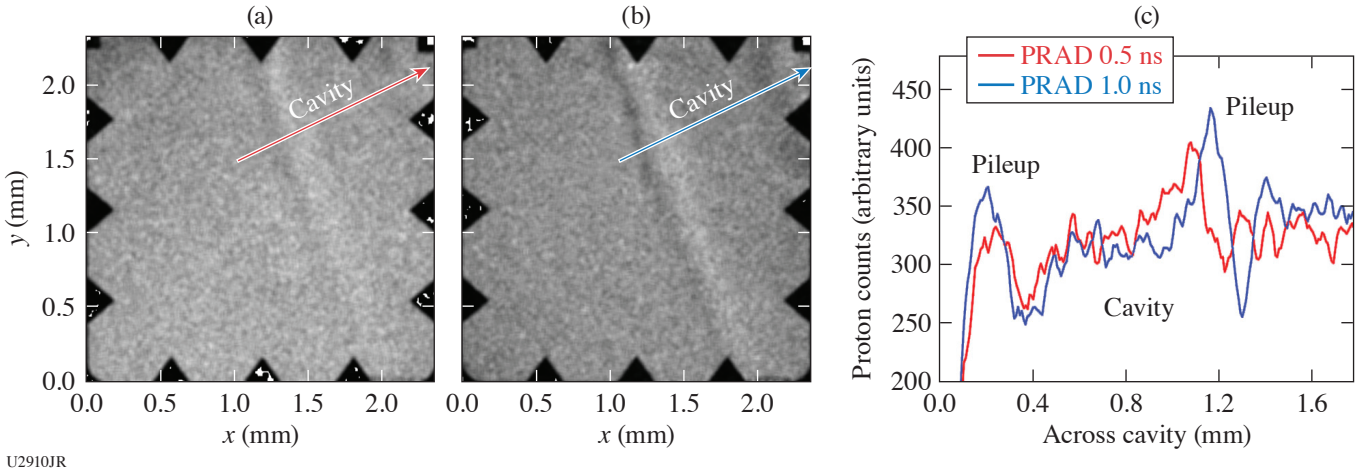

Figure 19
The raw proton radiography CR-39 images obtained with 15-MeV protons. PRAD acquired at (a) 0.5-ns and (b) 1-ns expansion time. (c) The lineout across the cavity obtained from at 0.5 ns (red curve) and 1 ns (blue curve). PRAD: proton radiography.

In summary, we have developed a novel experimental platform for benchmarking of Nernst effect in an open-geometry configuration at the Omega Laser Facility. We have successfully measured cavitation of magnetic fields by proton radiography and electron temperature and density, as well as bulk flow velocity at different positions across cavity by 2ω optical Thomson scattering. The preliminary analysis of proton radiography results indicates magnetic-field advection in time and pileup at the edges of the cavity. These results will be used for benchmarking extended magnetohydrodynamic codes. This platform can be also used to benchmark the Nernst effect in low- (high Nernst number $5 < N_e < 10$) and high-magnetization regimes ($0.1 < N_e$) by tuning magnetic field and gas-jet parameters.

Probing In-Flight Vacuum Magnetic-Field Compression on OMEGA

J. L. Peebles,* F. García-Rubio, J. R. Davies, D. H. Barnak, P. V. Heuer, and R. Betti
Laboratory for Laser Energetics, University of Rochester
*Principal Investigator

Measurements of the compression of a magnetic field have remained elusive in laser-driven magnetohydrodynamic (MHD) experiments. These measurements are required to validate simulations for field conservation and loss mechanisms. The primary goal of this campaign was to measure the magnetic field at different stages of compression in a cylindrical target, which would provide experimental feedback for MHD codes. To do this, an experiment was carried out where a strong magnetic field (>65 T) was applied to a cylindrical implosion with a large radius. This large radius (twice the size of a typical cylindrical implosion on OMEGA) was chosen to provide enough of a window for proton probing to be used. Prior issues with using proton probing to measure magnetic fields transverse to the primary field axis was that deflection was too large; to address this we probed down the axis of the cylinder, which has been proven to be a more-accurate measurement for fields of this magnitude. Ideally this probing could be done while the shell is in-flight, providing many data points on field strength and compression.

The experimental setup is shown in Fig. 20. The well-benchmarked cylindrical implosion setup used for MagLIF experiments was modified to drive a narrower portion of the cylinder. Since the cylinder was twice the radius of typical cylindrical experiments, intensity on target had to be maintained by doubling beams on a portion half the length of the typical MagLIF implosion. The tube was left empty of gas for ease of construction since field compression should occur regardless of fill. A D^3He exploding-pusher proton source was used to probe the interaction; since the drive for the exploding pusher and the cylinder needed to be the same pulse shape and the proton source benefits from shorter, higher-intensity pulses, there was a long coasting period for the compressing cylinder. An image plate placed on the wedge range filter module (WRFM) allowed for a simultaneous x-ray measurement of the mesh fiducial, which indicated the initial angle of the mesh without field deflections.

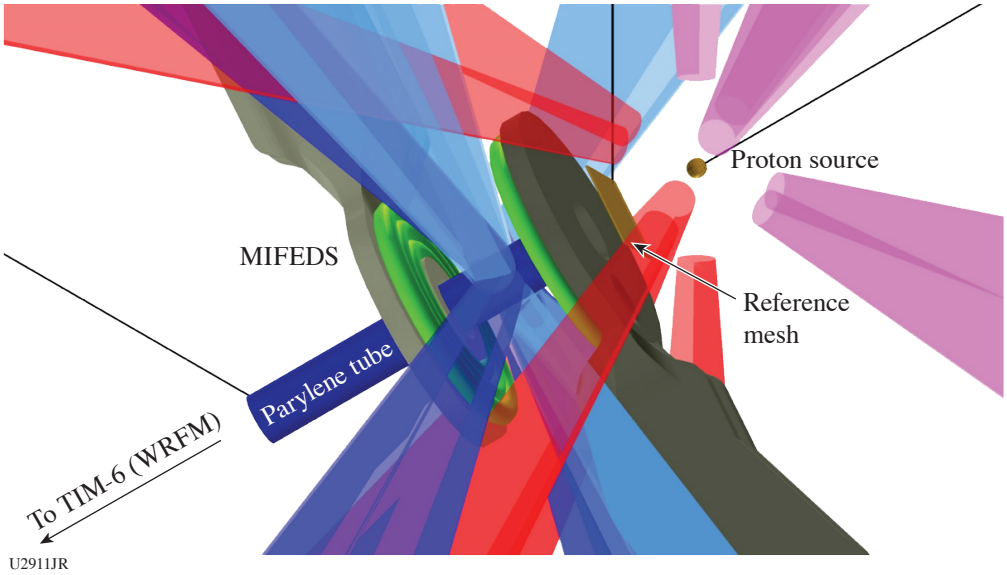

Figure 20
Schematic of the experimental setup. A large-radius cylindrical implosion is radiographed axially by protons, measuring the field applied by the MIFEDS coils.

Six shots were carried out in the campaign: three without the magnetic field and three shots with the magnetic field. The reference shots without the magnetic field were able to image the reference mesh at two different stages of compression. Since there was no field, the mesh appeared to be stable regardless of probe time, with the compressing shell scattering the protons later in time. As shown in Fig. 21, the mesh can be distinguished at nearly any stage of compression. X-ray framing camera data indicated that the shell coasts to full compression by 4.5 ns, where the probe at 3.5 ns can probe a region roughly 350 μm in diameter. Proton attenuation from scattering removes most of the signal from the regions where the shell has been in flight, although the proton signal appeared to decrease throughout the shot day (despite neutronics indicating otherwise).

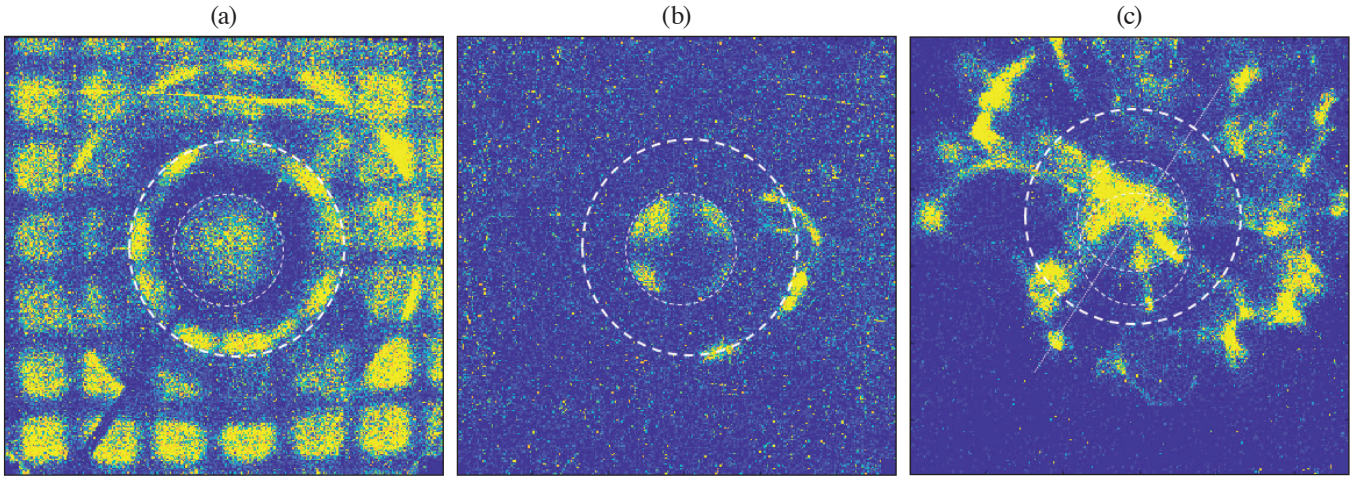

Figure 21
Proton probes of three different shots. The probes are timed at 1.0, 3.5, and 3.5 ns with the field off, off and on, and left to right, respectively. The grid is clearly distinguishable in the first two images, although at 3.5 ns the cylinder is nearly fully compressed. When the field is added, however, the mesh distorted beyond identifiability, even though the compression is at the same stage as the second image.

Difficulties with the MIFEDS led the diagnostic to be disqualified for use after the shot day since the unit entered a self-charge state when getting ready for the seventh shot and destroyed the target. For one of the magnetized shots, the reference mesh was apparently lost close to shot time (after the Target Viewing System was shuttered). Late timing of the proton probe for another magnetized shot led to missing the compressed field. This led to only one shot with usable magnetized data. Due to a mistiming of one of the MIFEDS units, the field was lower and asymmetric. Upon adding the external magnetic field, the very clear mesh was heavily distorted such that the angle of the mesh could not be identified. Fourier analysis indicated that some features may be aligned with a 37° rotation of the mesh; however, this appears unlikely since this would indicate much higher field compression than the shell at this stage could accomplish. While the field for this shot was not ideal, it alone does not explain the complete distortion of the radiograph. More likely, the ends of the field compression region are significantly more complex than an ideal compression.

For future shot days exploring field compression it would be of great benefit to have additional data points earlier in the compression. Presumably, field-distortion effects would not be so strong early into compression. By probing earlier in time, more of the mesh is visible on the probe, making the process of identifying mesh lines and angles much more likely. Other improvements would include shortening the length of the tube; the length of tube combined with the proximity to the proton source meant that two of the rings seen on the early time radiographs are the uncompressed regions of the tube close to and far away from the source. Shortening the tube to 1 to 2 mm (rather than 10+ mm) would shrink this feature substantially. Improvements made to the MIFEDS diagnostic since this shot day have also made its usage much more reliable.

This experiment was conducted at the Omega Laser Facility at the University of Rochester's Laboratory for Laser Energetics with the beam time through the Laboratory Basic Science program.

Electron Energization in Colliding and Reconnecting Magnetized Plasmas

M. J. Rosenberg,[1*] G. Fiksel,[2] W. Fox,[3] D. Schaeffer,[4] and C. K. Li[5]
[1]Laboratory for Laser Energetics, University of Rochester
[2]University of Michigan
[3]Princeton Plasma Physics Laboratory
[4]Princeton University
[5]Massachusetts Institute of Technology
[*]Principal Investigator

The MagRecon-22A shot day on OMEGA (17 February 2022) through the LBS Program successfully demonstrated an enhancement in the suprathermal electron population in laser-plasma experiments that drove the collision or reconnection of plasma plumes carrying self-generated magnetic fields. The energization of particles during the annihilation of magnetic fields is a common process in astrophysical plasmas, but is poorly understood and has rarely been investigated in the laboratory. The experiments use the interaction of 200-J, 0.5-ns laser pulses with 5-μm-thick CH foils to produce Biermann-battery magnetic fields that azimuthally encircle the expanding plasma created by each beam. While previous experiments[40] [illustrated schematically in Fig. 22(a)] showed that the interaction of two adjacent plasma plumes containing antiparallel magnetic fields, which undergo magnetic reconnection, enhanced the energetic electron population in the direction of the reconnection current sheet, it was not proven whether this was due to the collision or due to reconnection itself. To address this question, this shot day employed the configuration shown in Fig. 22(b), in which the experimental geometry is altered so that the magnetic fields are parallel in the collision region and do not reconnect.

The energized electron spectra are shown in Fig. 23. Preliminary analysis shows that experiments with colliding parallel fields produce significantly more than twice the energized electron population than experiments with only a single laser–foil interaction (and therefore no collision), indicating that the plasma plume collision contributes partially to the acceleration of electrons regardless of the magnetic-field orientation or any reconnection. In addition, the magnetic reconnection experiments show more electron energization than in experiments driving the collision of parallel magnetic fields, although there is significant shot-to-shot variation. These results suggest that the magnetized plasma plume collision causes some acceleration of electrons, possibly through a Fermi-like mechanism, but that magnetic reconnection is a significant contributor to electron energization. This platform can therefore be used in further experiments to study the dependence of magnetic reconnection-induced particle energization on reconnection parameters like collisionality.

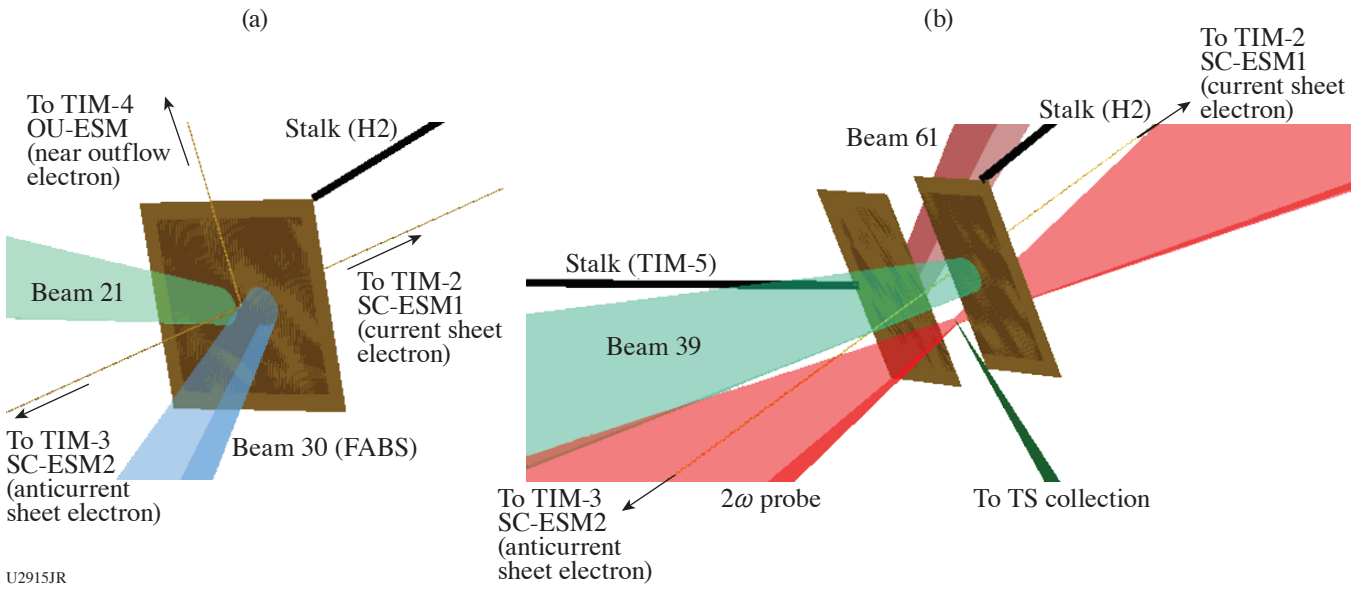

Figure 22
Experimental setup for (a) reconnection of anti-parallel magnetic fields and (b) collision (but no reconnection) of parallel magnetic fields. OU-ESM: Osaka University electron spectrometer; SC-ESM: single channel spectrometer; FABS: full-aperture backscatter station; TS: Thomson scattering.

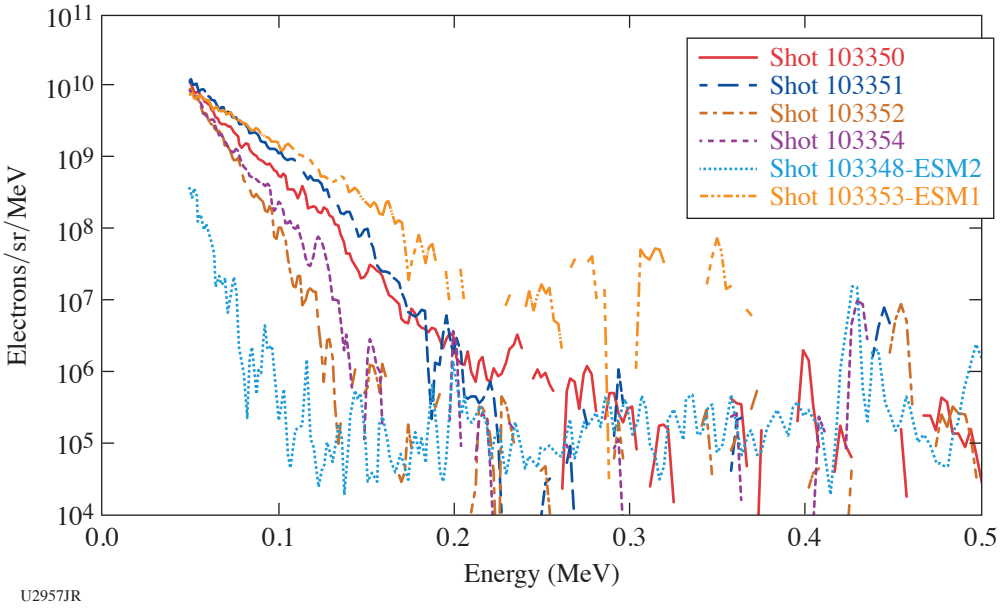

Figure 23
Measured energetic electron spectra for: one-beam experiments (no collision nor reconnection) (dashed curve), colliding parallel magnetic-field experiments (collision, but no reconnection) (thin solid curves), and reconnection (thick solid curves) experiments. The data have been background subtracted. The reconnection spectrum shows more energization than the parallel magnetic-field experiments (with significant variation).

These experiments were conducted at the Omega Laser Facility at the University of Rochester's Laboratory for Laser Energetics with the beam time through the Laboratory Basic Science Program.

Measuring Electron Densities in Nonlocal Thermodynamic Equilibrium Plasmas Using Isoelectronic Line Ratios

G. Pérez-Callejo,[1] E. V. Marley,[2] D. A. Liedahl,[2] J. A. Emig,[2] and M. B. Schneider[2*]
[1]Universidad de Valladolid, Spain
[2]Lawrence Livermore National Laboratory
[*]Principal Investigator

Measuring electron temperatures and densities in HED plasmas is no easy task. To that end, several different diagnostics have been designed, each exploiting one or several characteristics of these extreme plasmas, in order to extract information about their conditions. In particular, x-ray spectroscopy has proved to be a reliable diagnostic that can provide valuable information about the atomic structure of the elements in the plasma. A particularly bright component of the x-ray emission of HED plasmas is the He-like emission since He-like ions are present over a wide range of temperatures and densities. The brightest emission from these ions is, in most cases, the He_α complex, which comprises two He-like transitions and a significant contribution from Li-like ions. However, this complex is also heavily affected by optical depth effects, sensitive to gradients in the plasma, which makes it difficult to extract useful information (and usually other simpler lines are used).

In this experiment, we generated a uniform two-element plasma using a similar platform that was used in the past to characterize optical depth effects.[41] By placing a thin disk of CaS buried in a CH tamper, an axially expanding cylindrical plasma at 1 to 2 keV with $n_\mathrm{e} \sim 10^{21}$ cm^{-3} was generated. We recorded the x-ray emission spectra from both Ca and S, as well as the target size as a function of time. Since Ca and S are in the same proportion in the plasma, and at the same temperature and density conditions, the optical depth effects on their He_α emission are very similar and can be canceled out. This makes it possible to extract the electron density from the ratio $\left(w_\mathrm{s}/y_\mathrm{s}\right)/\left(w_{\mathrm{c}_\alpha}/y_{\mathrm{c}_\alpha}\right)$, where w and y are the two He-like transitions that make up the He_α emmission and the subindices are used to denote the element. All of the instruments obtained good data, which are currently being post-processed. Preliminary analysis of the data hints to the possibility that S dissolved into the target rather than staying confined to the buried layer (Fig. 24). This was a possibility since it was the first time that a salt-like component was used in this configuration, and target development was necessary. Careful post-processing of the spectral data is required to verify this possibility.

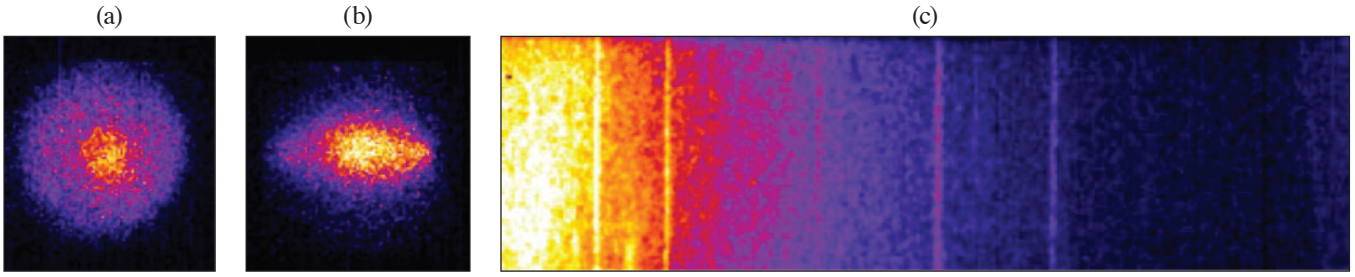

Figure 24
Example set of data from the experiment. (a) Top and (b) side view of the cylindrical plasma(c) S x-ray emission spectrum. The Ca spectrum was only obtained on film, which is currently being digitized.

This work was performed under the auspices of the U.S. Department of Energy by Lawrence Livermore National Laboratory under Contract DE-AC52-07NA27344. This document was prepared as an account of work sponsored by an agency of the United States government. Neither the United States government nor Lawrence Livermore National Security, LLC, nor any of their employees makes any warranty, expressed or implied, or assumes any legal liability or responsibility for the accuracy, completeness, or usefulness of any information, apparatus, product, or process disclosed, or represents that its use would not infringe privately owned rights. Reference herein to any specific commercial product, process, or service by trade name, trademark, manufacturer, or otherwise does not necessarily constitute or imply its endorsement, recommendation, or favoring by the United States government or Lawrence Livermore National Security, LLC. The views and opinions of authors expressed herein do not necessarily state or reflect those of the United States government or Lawrence Livermore National Security, LLC, and shall not be used for advertising or product endorsement purposes. The work has also been supported by the Research Grant No. PID2019-108764RB-I00 from the Spanish Ministry of Science and Innovation.

Probing the Fe–Ni Phase Space Using Powder X-Ray Diffraction Image Plates

S. M. Clarke,[1*] S. Singh,[1*] K. Bolduc,[2] and R. F. Smith[1]
[1]Lawrence Livermore National Laboratory
[2]University of Massachusetts, Amherst
[*]Principal Investigators

In this campaign we studied Fe–Ni, an alloyed material with geophysical relevance, under dynamic compression. The three goals to this experiment were to (1) determine the effect of Ni composition on the onset of melting on the Hugoniot, (2) understand the stability field of the γ [face-centered cubic (fcc)] phase within the alloy, and (3) develop a general methodology for investigating alloy materials under dynamic compression. Previous static compression experiments have shown that the incorporation of nickel expands the stability field of the fcc phase relative to the hexagonal close-packed (hcp) phase, thus changing the slope of the phase boundary.[42]

We successfully performed 13 shots: eight probing a shocked state and five probing a ramped state. For each shot we used one beam as a 2-ns x-ray backlighter and one beam to drive a shock- or ramp-compression wave in the sample. From the ramp-compression experiments, we found that alloying did not change the structure along the ramp quasi-isentrope. The Fe–Ni alloy maintained the hcp structure like the behavior of pure Fe. Preliminary analysis suggests we reached alloy densities over 15 g/cm^3. For the shock-compression samples, we targeted pressures near the melt line (see Fig. 25). Preliminary analysis suggests a diffraction signal consistent with melt in some shots, and a mixture of melt and high-pressure hcp phase in other shots. Pressure determination for these shots is ongoing, and when the analysis is complete, we will compare the onset of melt for the alloy to that of Fe to better understand the effect of alloying on the melt line. We do not observe the existence of a high-pressure bcc phase on the Hugoniot, in contrast to previous findings from other groups and theoretical predictions.[43] We hope to include all the data in a publication about the behavior of Fe–Ni alloys under dynamic compression.

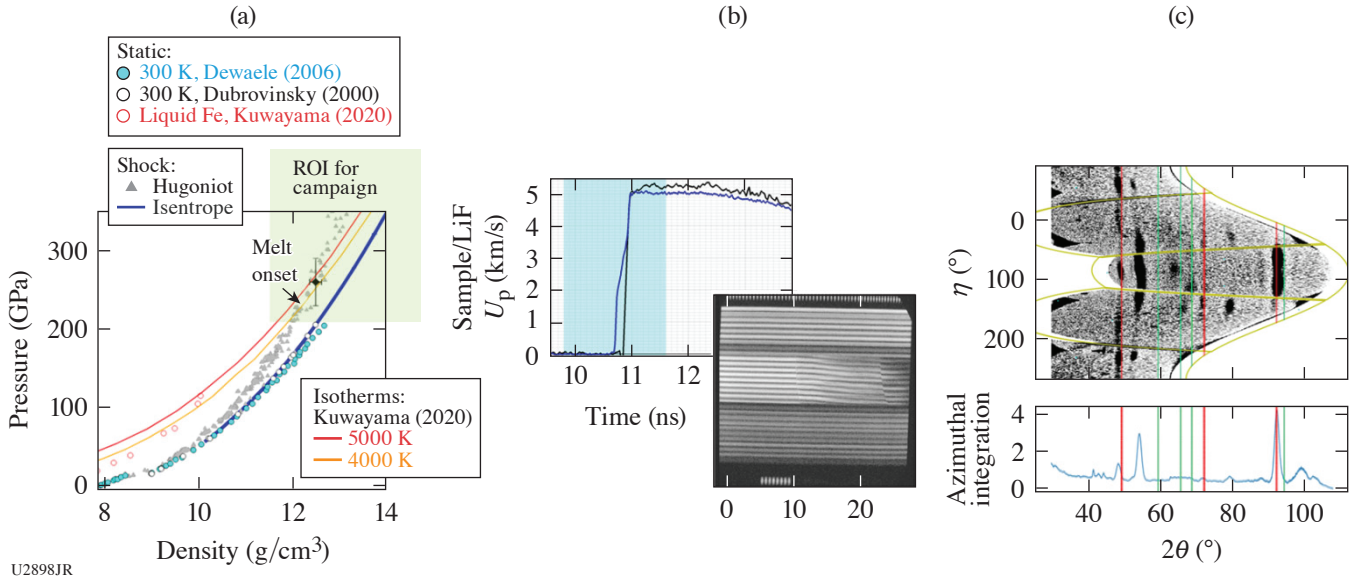

Figure 25
(a) Density versus pressure plot for Fe with the region of interest for this campaign highlighted in green. (b) Example of raw VISAR data and analyzed data showing the particle velocity at the sample/LiF interface, which can be used to determine the pressure in the sample. The blue highlighted region shows where the 2-ns x-ray pulse probed in time. (c) An example of analyzed data from the powder x-ray diffraction image-plate (PXRDIP) diagnostic. This diagnostic will provide information about the density and phase of the alloy on compression. ROI: region of interest.

This work was performed under the auspices of the U.S. Department of Energy by Lawrence Livermore National Laboratory under Contract DE-AC52-07NA27344.

Measuring the Viscosity of MgO at Lower-Mantle Conditions

R. F. Smith,[1*] T. Perez,[2] S. Ali,[1] P. M. Celliers,[1] F. Coppari,[1] J. H. Eggert,[1] and J. K. Wicks[2]
[1]Lawrence Livermore National Laboratory
[2]Department of Earth and Planetary Sciences, Johns Hopkins University
[*]Principal Investigator

The viscosity of MgO under high pressures and temperatures strongly influences a terrestrial planet's mantle dynamics, which impacts the planet's chemical and thermal evolution. Characterizing mantle dynamics is crucial in our understanding of the geologic history of planets in our solar system, as well as establishing habitability of exoplanetary systems. Despite the importance of MgO viscosity, there is currently no consensus from either theory or experiment on its value at mantle conditions. Here we use new experimental techniques to constrain the rheological properties of MgO at pressures and temperatures relevant to the Earth's mantle. The results of these experiments will constrain mantle dynamics models, aiding our understanding of planetary interior evolution and surface habitability.

The OMEGA EP laser ramp drive allows us to reach lower-mantle pressures over a wide range of strain rates while providing direct constraints of viscosity with the OMEGA EP active shock breakout (ASBO–VISAR) diagnostic. The target design for this experimental campaign is shown schematically in Fig. 26. Perturbed interfaces between ablation layer and sample create perturbed shock waves and Rayleigh–Taylor (RT) instabilities that can be tracked with VISAR to constrain rheological properties. An example of the data obtained is shown in Fig. 27. Our shot day was very successful and data analysis is ongoing.

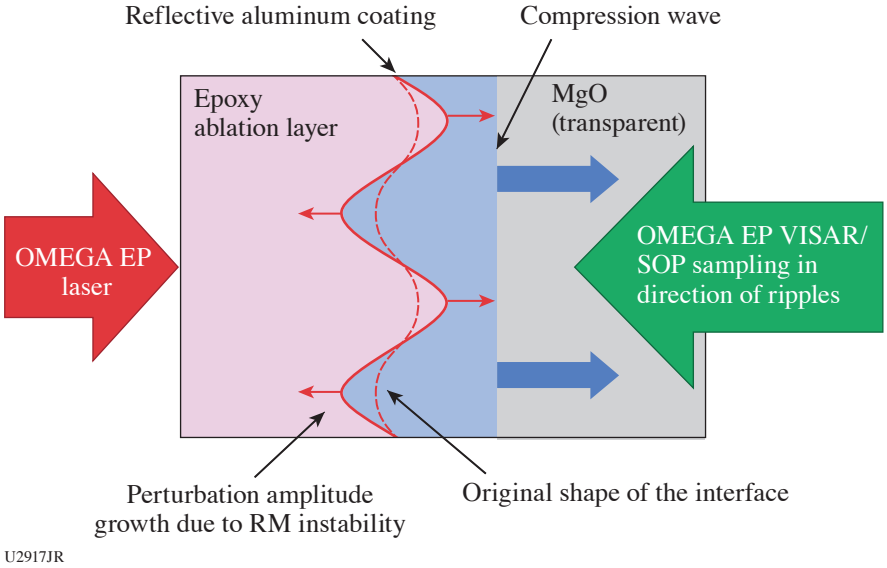

Figure 26
Conceptual design of viscosity measurements on OMEGA EP. The laser-ablated shock wave takes on sinusoidal shape after passing through rippled epoxy–MgO interface and undergoes damped oscillation controlled by viscosity. VISAR/SOP can track continuous breakout of ripple anti-node on wedged interface and therefore can constrain viscosity. RM: Richtmyer–Meskov.

This experiment was conducted at the Omega Laser Facility at the University of Rochester's Laboratory for Laser Energetics with the beam time through the Laboratory Basic Science program.

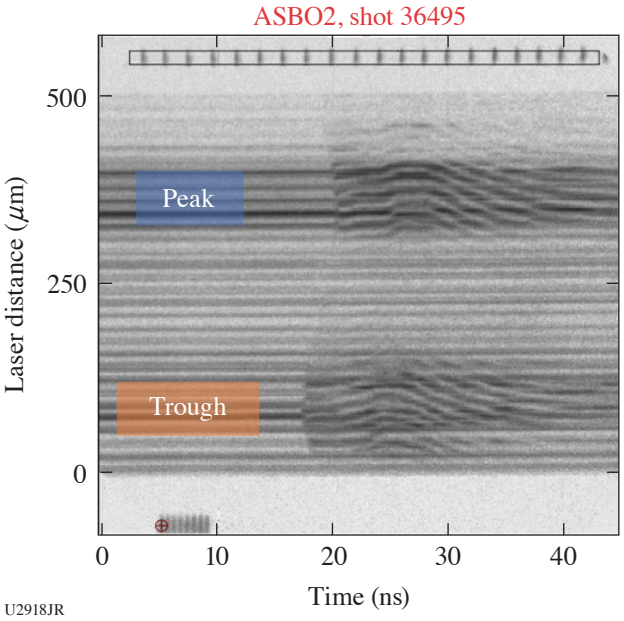

Figure 27
Example VISAR/ASBO data using the design from Fig. 26.

Studying the T–T Reaction at Energies Exceeding 2 MeV on OMEGA

A. Schwemmlein,[1*] C. Stoeckl,[1*] W. U. Schröder,[2] and W. T. Shmayda[1]
[1]Laboratory for Laser Energetics, University of Rochester
[2]Department of Chemistry, University of Rochester
[*]Principal Investigator

TNSA provides a unique opportunity to generate rare-isotope particle beams for nuclear-reaction experiments. Such experiments can be done at short-pulse laser facilities. In this technique, the surface of a small ($500 \times 500 \times 20$-μm^3) metallic converter foil is doped with the particle specie to be accelerated. When the foil is hit from the back with a high-power ($>10^{18}$ W/cm^2) laser pulse, particles from the foil surface layers are ejected and accelerated by the strong electric fields generated in the process. This approach is especially interesting for the generation of a beam of energetic tritons ($^3H^+$), which is presently not available anywhere. TNSA pilot studies on OMEGA EP[44,45] have generated beams of tritons capable of inducing nuclear reactions, for example, D–T fusion in a secondary, deuterated physics target. Utilizing this beam to study the tritium–tritium (T–T) reaction in a similar fashion can answer open questions about the predominant T–T reaction channel, as well as the structure of the compound nucleus ^{6}He. It is noteworthy that the tritium used in viable TNSA experiments is confined within small volumes of metal lattice and in amounts that are orders-of-magnitude smaller than in comparable accelerator experiments.

A follow-up experiment utilized improved converter and physics targets, each consisting of a stainless-steel substrate and an unpassivated 500-nm titanium layer. A radio-chemical analysis of the targets revealed a tritium content about 5× higher (670 μCi versus 130 μCi) compared to the pilot study. A control experiment with this type of converter foil and a secondary deuterated physics target produced the expected D–T fusion neutrons (see Fig. 28). However, the total neutron yield did not improve appreciably compared to the pilot study, suggesting that the additional tritium in the improved converter foil did not participate in the TNSA process.

A new experiment was conducted to study the triton-on-tritium (t–T) reaction. Here, the deuterated physics target was replaced with a tritiated physics target. The resulting spectrum of TT neutrons is compared in Fig. 28 with those of the D–T control reaction. The absence of neutrons above the background in the former spectrum is consistent with the much-lower T–T reaction cross section that was previously reported,[46] up to about $E_t \approx 1$ MeV. This new result is a first indication that the T–T reaction does not proceed via the third excited state of ^{6}He at 2.3 MeV above the T–T reaction threshold—an energy that could not be reached in past experiments. Like in the D–T reaction, which proceeds via ^{5}He, population of this ^{6}He state would noticeably increase the reaction cross section.

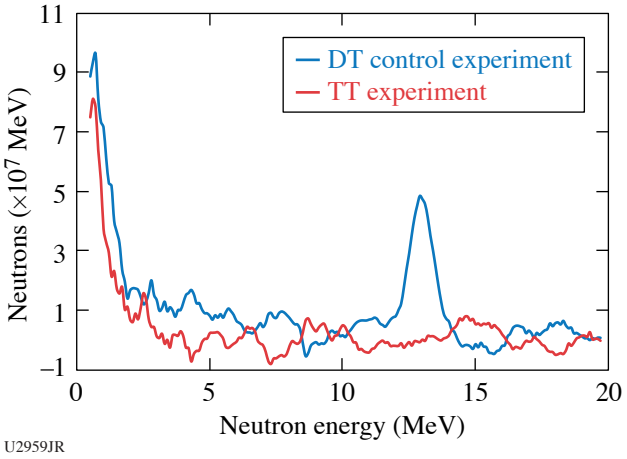

Figure 28
Neutron time-of-flight spectrum from the "8 × 4 nTOF" detector in energy space. While the TNSA triton beam generated a DT peak with a secondary deuterated target in the control experiment, no neutrons above the background were observed in the experiment with a secondary tritiated target.

These experiments were conducted at the Omega Laser Facility at the University of Rochester's Laboratory for Laser Energetics with the beam time through the Laboratory Basic Science Program.

Angular Momentum Transport in Disk-Jet Transitions

G. Swadling,[1*] F. Suzuki-Vidal,[2] V. Valenzuela-Villaseca,[2] M. Bailly-Grandvaux,[3] and C. Walsh[1]
[1]Lawrence Livermore National Laboratory
[2]Imperial College London, UK
[3]University of California, San Diego
[*]Principal Investigator

First experiments were performed on OMEGA looking at the formation of supersonic rotating plasmas as a platform to study fundamental HED hydrodynamics and laboratory astrophysics.[47] These experiments were part of the AngMomentumDisk-22A Campaign and were performed on 9 February 2022.

The experiments consisted of a target package made of six V-shaped apertures in a circular array with a diameter of ~12 mm [Fig. 29(a)], 3-D printed in CH. Each V-shaped target has a 5° tilt respect to the axis of the array, with each target "face" illuminated by a 3ω 500-ns, 1-ns square beam. This drives simultaneous radial plasma flows off-axis, injecting initial angular momentum and thus driving a rotating plasma.

The main diagnostic was optical Thomson scattering in spatially resolved mode, using 120 J with a duration of 3.7 ns. Scattered light was collected at 63° from the input **k** vector. Data consisted of IAW and EPW spectra. Example results are shown in Figs. 29(b) and 29(c) from 5 to 8.7 ns at a position −500 μm from the axis of the array. The results were very consistent for all shots. Analysis of the IAW spectra at 8 ns is shown in Fig. 29(d), which results in plasma parameters of the rotating plasma constrained by analysis of the EPW spectra at the same time. Plasma parameters are in line with 3-D numerical simulations with the *GORGON* code.[48]

The experiment was conducted at the Omega Laser Facility at the University of Rochester's Laboratory for Laser Energetics with the beam time through the Laboratory Basic Science (LBS) Program. Work was performed under the auspices of the U.S. DOE by LLNL under Contract DE-AC52-07NA27344. Research supported by The Royal Society through a University Research Fellowship.

1. M. Millot *et al.*, Nature **569**, 251 (2019).
2. M. Millot *et al.*, Nat. Phys. **14**, 297 (2018).
3. B. Cheng *et al.*, Nat. Phys. **17**, 1228 (2021).
4. Y.-J. Kim *et al.*, Sci. Rep. **11**, 5610 (2021).
5. S. Brygoo *et al.*, J. Appl. Phys. **118**, 195901 (2015).

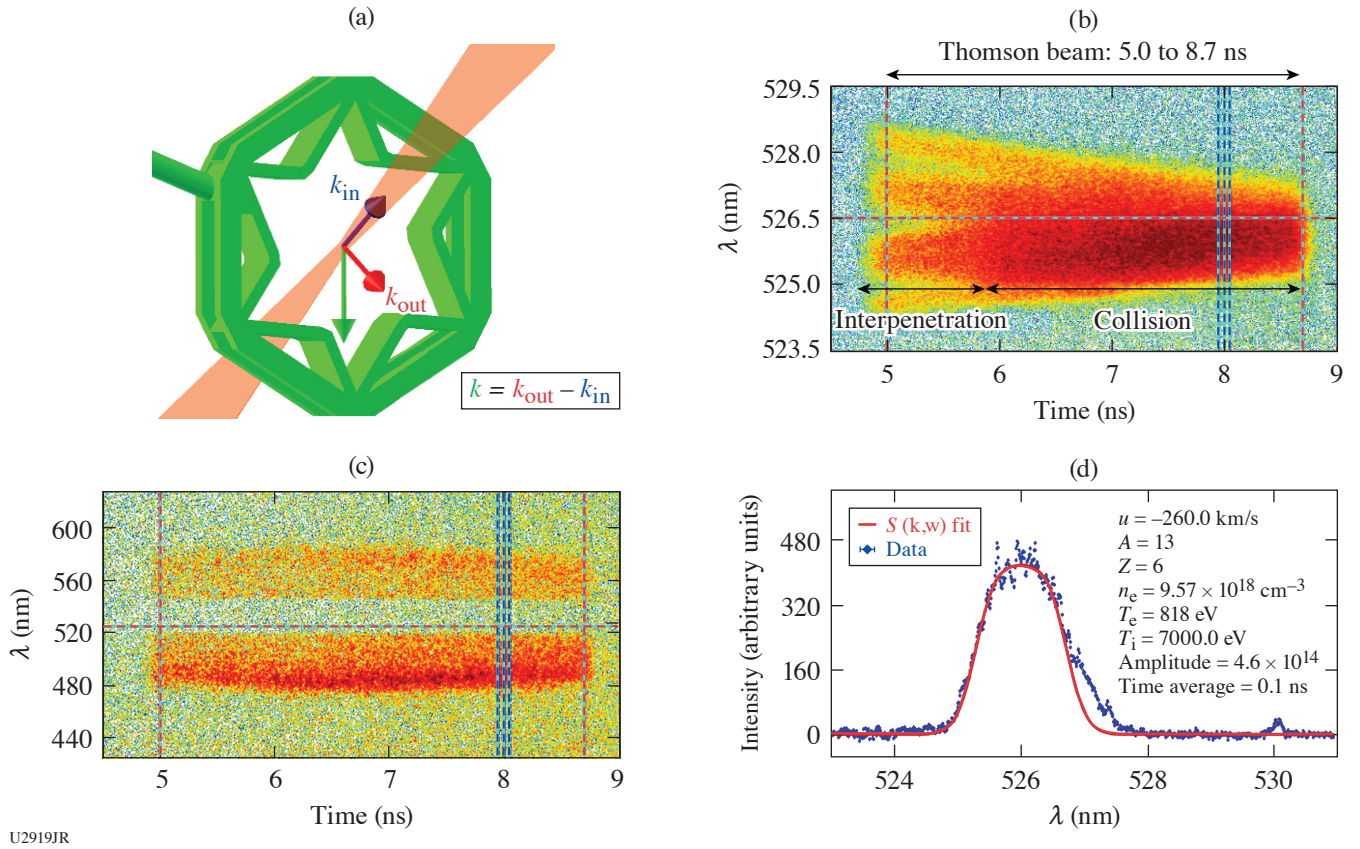

Figure 29
Overview of AngMomentumDisk-22A shot day. (a) *VISRAD* view of sixfold target with Thomson scattering geometry. [(b),(c)] Example results from Thomson scattering (shot 103212), EPW and IAW, respectively. Data were obtained from 5 to 8.7 ns after the beams illuminated the targets. (d) Lineout from IAW data at 8 ns, integrated over 100 ps together with a fit of the theoretical spectral density function $S(k,w)$, which allows measuring plasma parameters in the rotating plasma.

6. Y.-J. Kim *et al.*, Phys. Rev. Lett. **129**, 015701 (2022).
7. L. Gao *et al.*, Phys. Plasmas **23**, 043106 (2016).
8. A. Chien *et al.*, Nat. Phys. **19**, 254 (2023).
9. D. J. Stark, T. Toncian, and A. V. Arefiev, Phys. Rev. Lett. **116**, 185003 (2016).
10. H. G. Rinderknecht *et al.*, New J. Phys. **23**, 095009 (2021).
11. F. Spite and M. Spite, Astron. Astrophys. **115**, 357 (1982).
12. M. Tegmark *et al.*, Phys. Rev. D **69**, 103501 (2004).
13. S. Burles *et al.*, Phys. Rev. Lett. **82**, 4176 (1999).
14. A. B. Zylstra *et al.*, Rev. Sci. Instrum. **90**, 123504 (2019).
15. G. Q. Liao and Y. T. Li, IEEE Trans. Plasma Sci. **47**, 3002 (2019).
16. G. Liao *et al.*, Proc. Natl. Acad. Sci. **116**, 3994 (2019).
17. S. Herzer *et al.*, New J. Phys. **20**, 063019 (2018).
18. K. Y. Kim, University of Maryland, College Park, MD, Technical Report DOE-UMCP-3891 (5 May 2016).
19. G.-Q. Liao *et al.*, Phys. Rev. X **10**, 031062 (2020).
20. Y. Zeng *et al.*, Opt. Express **28**, 15258 (2020).
21. E. Wigner and H. B. Huntington, J. Chem. Phys. **3**, 764 (1935).
22. J. M. McMahon and D. M. Ceperley, Phys. Rev. B **84** (14), 144515 (2011); **85** (21), 219902(E) (2011).)
23. B. M. Haines *et al.*, Phys. Plasmas **21**, 092306 (2014).
24. L. V. Al'tshuler, S. E. Brusnikin, and E. A. Kuz'menkov, J. Appl. Mech. Tech. Phys. **28**, 129 (1987).

25. V. N. Goncharov *et al.*, Phys. Rev. Lett. **125**, 065001 (2020).
26. T. R. Boehly *et al.*, Opt. Commun. **133**, 495 (1997).
27. S. Ressel *et al.*, Phys. Plasmas **29**, 072713 (2022).
28. C. Stoeckl *et al.*, Rev. Sci. Instrum. **87**, 11E323 (2016).
29. D. T. Michel *et al.*, Rev. Sci. Instrum. **83**, 10E530 (2012).
30. I. V. Igumenshchev *et al.*, Phys. Plasmas **23**, 052702 (2016); A. Colaïtis *et al.*, J. Comput. Phys. **443**, 110537 (2021).
31. C. E. Parker, "The ^{3}H(d, γ) Reaction and the ^{3}H(d, γ)/^{3}H(d, n) Branching Ratio for $E_{\text{c.m.}} \leq 300$ keV," Ph.D. Thesis, Ohio University, 2016.
32. Y. Kim *et al.*, Phys. Rev. C **85**, 061601 (2012).
33. J. Jeet *et al.*, Phys. Rev. C **104**, 054611 (2021).
34. A. Nishiguchi *et al.*, Phys. Rev. Lett. **53**, 262 (1984).
35. S. A. Slutz *et al.*, Phys. Plasmas **17**, 056303 (2010).
36. M. R. Gomez *et al.*, Phys. Rev. Lett. **125**, 155002 (2020).
37. C. A. Walsh *et al.*, Phys. Rev. Lett. **118**, 155001 (2017).
38. C. Ahdida *et al.*, Front. Phys. **9**, 788253 (2022).
39. M. R. Weis *et al.*, Phys. Plasmas **28**, 012705 (2021).
40. G. Fiksel *et al.*, J. Plasma Phys. **87**, 905870411 (2021).
41. G. Pérez-Callejo *et al.*, Phys. Rev. Lett. **126**, 085001 (2021).
42. T. Komabayashi, K. Hirose, and Y. Ohishi, Phys. Chem. Miner. **39**, 329 (2012).
43. L. Dubrovinsky *et al.*, Science **316**, 1880 (2007).
44. A. K. Schwemmlein *et al.*, Nucl. Instrum. Methods Phys. Res. B **522**, 27 (2022).
45. C. Stoeckl *et al.*, Nucl. Instrum. Methods Phys. Res. B **453**, 41 (2019).
46. C. Wong, J. D. Anderson, and J. W. McClure, Nucl. Phys. **71**, 106 (1965).
47. D. D. Ryutov, Astrophys. Space Sci. **336**, 21 (2011).
48. A. Ciardi *et al.*, Phys. Plasmas **14**, 056501 (2007).